

Process for Optimizing Optical Coupling between Fibers and Photonic Integrated Circuits

A senior design project submitted in partial fulfillment of the requirements
for the degree of Bachelor of Science at Harvard University

Alexander Giglio
S.B. Candidate in Mechanical Engineering

Thesis Reader: Marko Lončar
Advisor: Eric Puma

Harvard University John A. Paulson School of Engineering and Applied
Sciences
Cambridge, MA
April 10, 2019

Abstract

Process for Optimizing Optical Coupling between Fibers and Photonic Integrated Circuits

Alexander Giglio

The Laboratory for Nanoscale Optics (LNO) at Harvard University researches and develops quantum optics, which are devices that can manipulate single photons. Quantum optics experiments on photonic integrated circuits (PIC) are very sensitive to the insertion losses created when transmitting a mode from an optical fiber to the PIC. This project aims to develop a process that will enable the LNO to optically couple fibers to PICs with sufficiently low losses and mechanically fasten the components together. Novel PIC architecture is leveraged to create the geometric conditions necessary for achieving alignment of a linear fiber array with a linear waveguide array on a PIC. The nanopositioning stage control program developed for this project automatically achieves optimal alignment in both translation and rotation using a single photodiode power meter and open-source software. Optimal alignment between an optical fiber and PIC waveguide is achieved in five minutes.

Declaration

I hereby submit this thesis in partial fulfillment of the requirements for the degree of Bachelor of Science in Mechanical Engineering at Harvard University.

Acknowledgments

I thank my thesis reader Marko Lončar for giving me the opportunity to work on this project.

I thank my thesis advisor Eric Puma being a steady source of guidance and encouragement. You remained patient when I submitted all my assignments late, and you helped make this project a worthwhile experience.

I thank my section leader and ADUS Chris Lombardo for providing invaluable feedback on my assignments and for making sure I graduate.

I thank Graham Joe, CJ Xin, and everyone else in the Lončar group that helped me overcome hurdles and made this project possible.

I thank Steve Cortesa, Elaine Kristant, and Tony Turner for listening to me complain about my thesis for the entirety of senior year.

I thank the engineering students of the Class of 2020 for their emotional support while we worked on our theses together. ES 100? More like ES *Fun*hundred.

I thank the Harvard College Human Powered Vehicle Team: all the new members for their enthusiasm, the officers for their hard work, and Evelyn Hu for being better than any advisor we could imagine.

I thank baseball for teaching me to be comfortable in a two-strike count.

And I thank my all my friends and family who kept me sane.

Contents

1	Introduction	8
1.1	Motivation and Problem Statement	8
1.2	Background	10
1.2.1	Coupling approaches	10
1.2.2	Packaging	11
2	Design	14
2.1	Design goals	14
2.2	Technical specifications	15
2.2.1	Design for fabrication	15
2.2.2	Design for speed	15
2.2.3	Alignment precision	15
2.2.4	Thermal stability	15
2.2.5	Technical specifications summary	16
2.3	Design constraints	17
2.3.1	PIC materials and geometry	17
2.3.2	Fiber optics	17
2.3.3	Size constraints	17
2.4	Design approach	18
2.4.1	Overview	18
2.4.2	Edge coupling	18
2.4.3	PIC architecture	19
2.5	Component selection	22
2.5.1	Interposer	22
2.5.2	Nanopositioning stage	22
2.5.3	Photodiode and power meter	23
2.5.4	Light source and controller	24
2.6	Simulation	25
2.6.1	2D FDE	25
2.6.2	2.5D varFDTD	26
2.7	Control software	28
2.7.1	First light	28
2.7.2	Translation optimization	29
2.7.3	Rotation optimization	29
2.7.4	Maintain alignment	29

2.8	Packaging	30
3	Build	31
3.1	Software	31
3.1.1	Stage control module	31
3.1.2	Taking measurements	32
3.2	Hardware	33
4	Measurement	35
4.1	Interposer-to-fiber coupling	35
4.2	Interposer-to-PIC coupling	38
4.2.1	Path dependence	39
5	Conclusion	41
5.1	Evaluation	41
5.2	Next steps	41
A	Technical specifications of nanopositioning stage	47
B	Drawings of interposer clamp	52
C	Technical specifications of photodiode and power meter	56
D	Lumerical Scripts	59
D.1	Geometry generation	59
D.2	FDE scripting	62
D.3	varFDTD scripting	63
E	Python module for interfacing with the nanopositioning stage	65

List of Figures

1.1	Schematic of edge coupling to a silicon PIC using a lensed fiber and mode converter [5]	10
1.2	Schematic of a 1D grating coupler for inserting light into a fiber from a silicon PIC [4]	11
1.3	Schematic of a V-groove fiber holder integrated into an edge coupler with an inverted taper waveguide (not to scale)	12
1.4	Micrograph of lensed fiber fixed in place via laser welding [8]	13
2.1	Cross section of a typical LiNbO ₃ waveguide	17
2.2	System diagram	18
2.3	Schematic of a PIC with a splitting waveguide for measuring coupling	19
2.4	Potential PIC architecture for coupling with a single fiber in a fiber array	20
2.5	Potential PIC architecture for coupling with arbitrarily many fibers in a fiber array	20
2.6	PIC architecture for coupling with arbitrarily many fibers in an array using a single light source and power meter	21
2.7	Schematic of of LioniX fiber array device with interposer	22
2.8	Example of a XYZ manual micrometer stage [10]	22
2.9	Exploded view of interposer clamp	23
2.10	Layout of clamp and interposer on nanopositioning stage. Note the left-handed coordinate system of the stage.	24
2.11	Screenshots from Lumerical simulation	25
2.12	Results of FDE simulation	26
2.13	Results of varFDTD simulations in two planes	27
2.14	View along z -axis of waveguide cross sections and first light search path	28
3.1	Photograph of an interposer-PIC coupling setup	33
3.2	Micrograph of lensed fiber coupled to interposer	34
3.3	Composite false-color micrograph of PIC showing waveguide design	34
4.1	Schematic of fiber-to-interposer coupling with a lensed fiber	35
4.2	The two kinds of fibers employed for attempting interposer-to-fiber coupling	35
4.3	Finding the local maximum of coupling efficiency between a lensed facet fiber and the interposer on the xy -plane with a large z -displacement. Note the decrease in search space size going from left to right.	36

4.4	Left: A visualization of the search path of the interposer head. Right: The evolution of coupling efficiency between the lensed fiber and the interposer over time.	36
4.5	Measured best coupling efficiency while moving interposer closer to fibers after optimizing alignment in <i>xy</i> -plane	37
4.6	Schematic of two-point interposer-to-PIC coupling with U-shaped waveguide architecture.	38
4.7	480 $\mu\text{m} \times 150 \mu\text{m}$ sweep of interposer on <i>xy</i> -plane	38
4.8	Detail of Figure 4.7 with a circular region that could be evidence of coupling.	39
4.9	Difference in reflection pattern recorded depending on direction of zig-zags	39
4.10	Demonstration of the elimination of banding pattern due to random path	40
5.1	Three-step process for using two single-point couplings to achieve coupling along an arbitrarily large linear array	42

Chapter 1

Introduction

1.1 Motivation and Problem Statement

The Laboratory for Nanoscale Optics (LNO) at Harvard’s John A. Paulson School of Engineering and Applied Sciences (SEAS) is designing and producing quantum photonic devices. Quantum photonic devices are designed with specialized geometries and materials to create light-matter interactions that allow for the manipulation of single photons. Quantum photonic devices are a subset of wave optical devices, which manipulate light using physical structures with sizes comparable to the wavelength of the light in question.

A confluence of physical factors has resulted in these devices being very small. The signal attenuation of light near 1550 nm wavelength through silica optical fibers can be as low as 0.17 dB/km, making it ideal for telecommunications [1]. In order for an optical device to manipulate telecom wavelength infrared light as waves and not rays, its features need to have characteristic lengths on the order of 1 μm . Fabrication of devices at this scale has been enabled by existing CMOS technology developed to produce semiconductor devices like transistors [2]. Wave optics devices can perform passive functions like multiplexing via grating structures or active functions like signal modulation. A number of functional subcomponents can be combined on a single device or “chip” to perform a more complex function. These devices are called photonic integrated circuits (PICs) and are optical analogs of the more common electronic integrated circuits.

In many scenarios, the light source for PICs must be external. For example, the PIC could be a signal demultiplexer in a larger telecommunications network, so it has to receive a signal from long-distance optical fiber. For spatially-constrained setups, like those in research laboratories, PIC light sources are external for convenience and simplicity. Integrating a light source onto a PIC increases manufacturing complexity, and the most common PIC material, silicon, makes for an inefficient light source because of its indirect band gap [2]. An external light source, on the other hand, can be used for multiple PICs, and frees up space on a PIC that would otherwise be used for an integrated light source. In the LNO, light from a laser source is typically inserted into PICs via an optical fiber.

Inserting a signal from an optical fiber to a PIC is non-trivial. The mode field diameter (MFD) of a single-mode telecom-wavelength optical fiber is approximately 10 μm , whereas the MFD of a PIC waveguide is approximately 1 μm . Even with optimized geometries, the

coupling efficiency between an optical fiber and PIC waveguide is very sensitive to the relative orientation of the components because of the large mode size mismatch. The difficulties of optically coupling fibers with PICs are not only a consequence of mode size mismatch but also a result of the scale of the devices. At the micron scale, thermal expansion effects become significant, and conventional mechanical positioning methods like micrometer or stepper motor stages struggle to adjust with adequate precision. Even when a laboratory setup has the thermal stability and mechanical precision to theoretically achieve the desired alignment of components, manually actuating a micrometer stage and reading from a power meter to determine the level of optical coupling is slow and requires a good deal of practice. Once alignment is achieved, the fibers must be mechanically fastened together and packaged if the device is to be used in a different environment like a dilution refrigerator.

The LNO currently has no repeatable process for efficiently optically coupling optical fibers to their PICs for quantum optics experiments and maintaining coupling by packaging the components together. The inability to efficiently couple fiber optics to PICs is a limiting factor for quantum optics experiments because of their inherent high sensitivity to photon loss. Sourcing single photons for manipulating quantum states becomes effectively impossible when insertion losses cross a certain threshold [3]. This project aims to enable the LNO to quickly achieve efficient coupling in their laboratory by developing a process for aligning optical fibers with PICs and then mechanically joining them to maintain that alignment.

1.2 Background

1.2.1 Coupling approaches

There are two common approaches to achieving optical coupling between fiber optics and PICs: edge coupling and grating coupling. These approaches differ in how the optical fiber must be oriented relative to the planar surface of the PIC and the axes of its waveguides.

Edge Coupling

Edge coupling, also called “in-plane,” “end-fire,” and “butt” coupling, refers to configurations in which the fiber is in the plane of the PIC and coupled to a waveguide sharing the same central axis as the fiber. The mode propagates from the fiber to the PIC waveguide, or vice-versa, along a single axis [4]. Edge coupling is most commonly used for the commercial packaging of laser devices and is less common for semiconductor integrated photonics because of the extra manufacturing steps necessary. Some of these manufacturing steps include adding mode converters and polishing the edge of the PIC to optical quality [5].

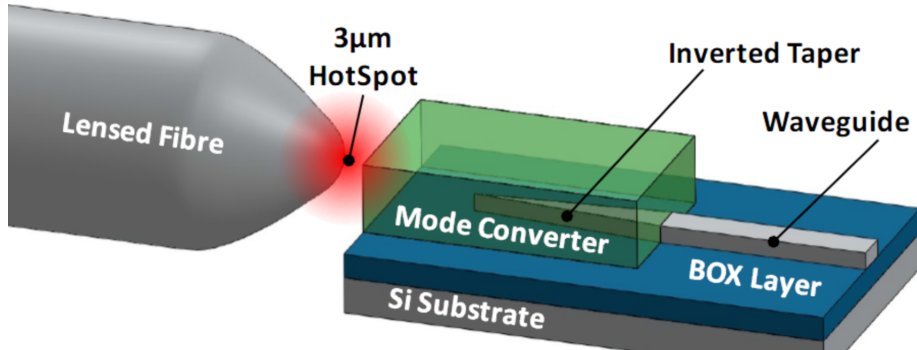


Figure 1.1: Schematic of edge coupling to a silicon PIC using a lensed fiber and mode converter [5]

Edge coupling can achieve the lower insertion losses of the two approaches discussed. A system like the one described in Figure 1.1 utilizes three common features to minimize losses: a lensed fiber with a conical tip that focuses the light in a Gaussian waveform with a small beam waist, cutting down mode size mismatch between the PIC waveguide and the fiber optic significantly; a mode converter that increases the MFD of the waveguide at the edge of the device to increase the tolerance for misalignment; and an inverted taper at the end of the PIC waveguide that decreases the confinement of the mode gradually along the axis of propagation [5]. Coupling efficiencies of -1 dB have been achieved with edge coupling, but the approach is very sensitive to misalignment, with the 1 dB bandwidth with respect to misalignment being $\pm 1.2 \mu\text{m}$ [4]. On LiNbO₃ integrated photonics with bilayer inverted tapers and a lensed fiber, the LNO has achieved -1.7 dB edge coupling efficiency [6].

Besides the introduced manufacturing complexity of adding a mode converter and the cost of using lensed fibers, edge coupling can conflict with space constraints. The optical

fiber must be in the plane of the PIC, and the insertion point must be on the edge of the chip, limiting the topology of devices [4].

Grating Coupling

Also called vertical coupling, grating coupling involves diffraction grating structures that utilize the Bragg diffraction phenomenon to change the direction of propagation of modes.

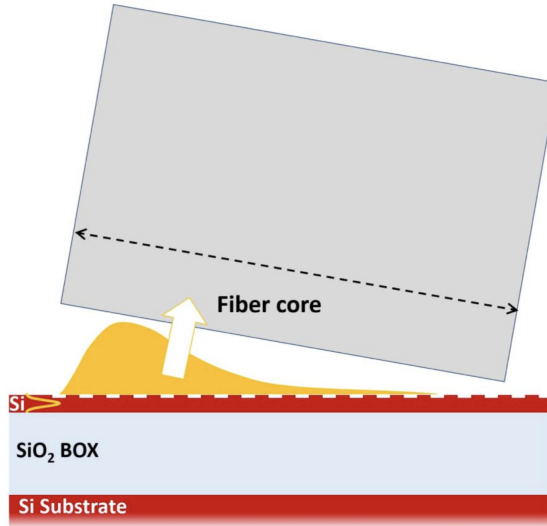


Figure 1.2: Schematic of a 1D grating coupler for inserting light into a fiber from a silicon PIC [4]

These grating structures are rows of ridges and trenches in the optical medium, and they require less post-fabrication processing than the structures required for edge coupling [4]. Grating coupling is called vertical coupling because the optical fiber's central axis is “vertical,” oriented roughly perpendicular to the horizontal plane of the PIC. An advantage of this orientation is that the grating coupler, which either accepts or emits a signal, can be located anywhere on the device, increasing the flexibility of PIC design with grating couplers.

Much the opposite of edge couplers in terms of misalignment tolerance, grating couplers can tolerate a greater misalignment due to the fact that the grating structures are designed with a footprint that matches the MFD of fiber optics. The 1 dB bandwidth with respect to misalignment for grating couplers is $\pm 2.5 \mu\text{m}$, about twice that of edge couplers. Inherent to the physics of diffraction, however, are greater energy losses. The best coupling efficiency for grating couplers is -1.6 dB [5].

1.2.2 Packaging

Once a coupling approach has been selected, the PIC and circuit can be aligned and packaged to become a single photonic device. The packaging of a photonic device can serve a number of functions, the most relevant of which to this project are mechanical fastening and thermal stabilization.

Fibers and PICs can be aligned using a passive structure, like a mechanical splice or fiber holder. For edge couplers, the PIC can be designed with a micromachined V-groove in its substrate that holds the fiber at the precise orientation for optimal coupling, as depicted in Figure 1.3. A silicon V-groove fiber alignment system can expect 1.3 μm of misalignment on the higher end [7].

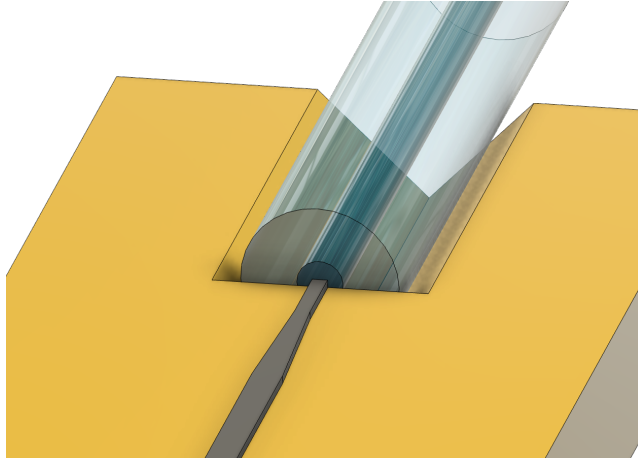


Figure 1.3: Schematic of a V-groove fiber holder integrated into an edge coupler with an inverted taper waveguide (not to scale)

For devices where it is not possible to build a mechanical fiber alignment feature into the PIC, active alignment processes are used. Active alignment processes typically use piezoelectric motors and flexure stages to orient components with respect to each other. For fiber-to-PIC coupling, the LNO manually aligns components, but there are devices like fusion splicers that can automatically achieve the optimal alignment between two components.

Once the components have been satisfactorily aligned, they need to be mechanically fastened. The simplest method is to use an index-matched adhesive, such as epoxy resin, to bond the fiber directly to the PIC. One benefit of this method is that the adhesive can rest directly between the fiber and PIC waveguide and reduce reflections that otherwise would result if there had been air between the two components.

A more complicated method, shown in Figure 1.4, is to laser weld a metal ferrule that surrounds the fiber optic to the device enclosure. Kovar metal, an iron-nickel-cobalt alloy, is a common choice for photonics enclosures because its thermal expansion coefficient matches that of the glass in optical fibers and thus minimizes misalignment due to temperature changes. Even with an enclosure that expands with the glass fiber, it is possible to include thermoelectric coolers in the package in order to maintain a constant temperature and further minimize misalignment due to temperature change. An advantage of the laser-welded ferrule approach is that its long-term alignment drift is smaller than that in epoxy bonds [5]. An experimental approach that the LNO is examining for diamond photonics is direct laser welding of a tapered fiber to the PIC, although this method has not yet been proven.

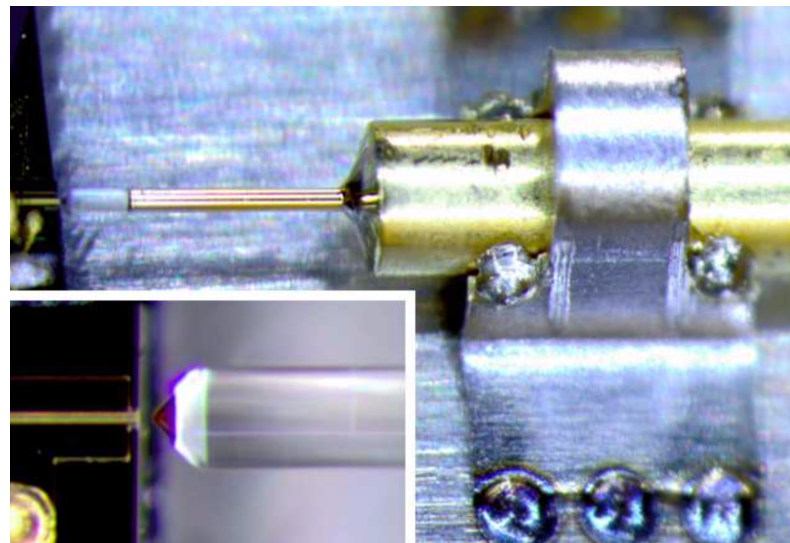


Figure 1.4: Micrograph of lensed fiber fixed in place via laser welding [8]

Chapter 2

Design

2.1 Design goals

The first goal of this project is to automate the optical coupling search process. Currently, when a scientist in the LNO wants to couple a fiber to their chip, they have to manually control a nanopositioning stage while staring at a power meter and microscope video feed and hope that they achieve any demonstrable level of coupling. This process is time-intensive searching in the dark that can be offloaded to a computer that searches the configuration space more quickly and reliably than a human user.

The second goal is to automate the alignment refinement process in order to optimize coupling. While a human user might be able to sufficiently optimize the position of a single fiber with respect to a PIC in an acceptable amount of time, nobody in the LNO has been able to couple multiple fibers to a single PIC simultaneously and optimize the alignment in all three degrees of rotation. The final process is intended to achieve both higher coupling efficiency than a human can and do so for multiple fibers at once.

The third goal is to develop a reliable means for mechanically fastening the optical fibers and PICs together in a single device. The fastening system needs to be reliable in the sense that the finished product maintains the optimized level of pre-fastening coupling while withstanding handling and temperature changes.

With all these goals comes the understanding that the finished process must be user-friendly and flexible. It needs to have room to grow and adapt as more is learned about quantum optics and as the needs of the LNO change over time.

2.2 Technical specifications

2.2.1 Design for fabrication

Any devices or machines necessary to fabricate parts for this process or to physically achieve alignment must be on Harvard’s campus or easily purchased from retailers. The process has limited utility if it requires more time, effort, and resources than the existing manual alignment process, so it makes sense to keep the manufacturing process localized and streamlined.

2.2.2 Design for speed

The computer-automated portions of the alignment process should achieve the desired alignment in under 16 hours. This number is based on the time that human operators take to align photonic devices and the fact that an automated process would be better if it could be run overnight.

2.2.3 Alignment precision

Fiber-to-PIC coupling efficiency is a function of not only relative spatial orientation but also the PIC’s architecture and the fabrication quality of the components involved. Even if the process can achieve optimal alignment, coupling efficiency will be below the threshold necessary for successful quantum experiments if the PIC’s facets aren’t properly polished or the fiber optic is dirty. As a result, this process must achieve alignment precision but does not need to breach a coupling efficiency threshold on prototype materials. Since $\pm 1.2 \mu\text{m}$ is the misalignment threshold for less than 1 dB insertion loss, the process should be able to achieve spatial alignment within $1.2 \mu\text{m}$ of optimal. This can be measured by perturbing the setup about the achieved maximum and demonstrating that there is no perturbation greater than $1.2 \mu\text{m}$ that increases the coupling efficiency.

2.2.4 Thermal stability

The mechanically fastened device must be able to maintain coupling efficiency within 1 dB of the highest coupling efficiency recorded over a 10°C temperature variation range. A completed device should remain functional in the LNO’s room temperature climate so that scientists may use it freely. Verification of this specification will require recording maximum coupling efficiency achieved during the alignment process as well as the device temperature during alignment.

2.2.5 Technical specifications summary

Specification	Quantity
Fabrication	Keep fabrication process on Harvard's campus
Speed	Achieve alignment in under 16 hours
Alignment precision	Achieve alignment within $\pm 1.2 \mu\text{m}$ of optimal
Thermal stability	Maintain $\pm 1.2 \mu\text{m}$ alignment tolerance over 10 °C variation

2.3 Design constraints

2.3.1 PIC materials and geometry

While PICs are most commonly made from silicon, the LNO is developing LiNbO₃ PICs to take advantage of its interesting properties, which include confinement of light in small waveguides and a strong electro-optic effect that can switch and modulate single photons [9]. To align with the current research in the LNO, PICs will be made using LiNbO₃. The cross-sectional geometry of the waveguides on prototype PICs, depicted in Figure 2.1, will reflect those of typical LNO PICs.

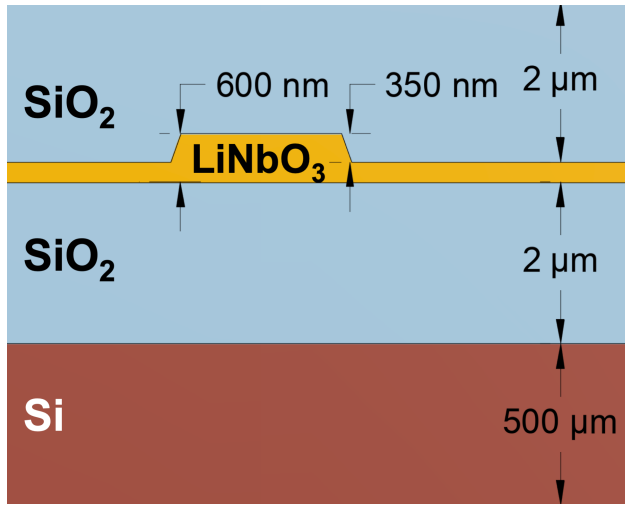


Figure 2.1: Cross section of a typical LiNbO₃ waveguide

The PIC are built on silicon handle wafers, depicted in brown in Figure 2.1. The bottom and cladding oxide layers, depicted in light blue, sandwich a layer of LiNbO₃, depicted in yellow. The lower refractive index of the oxide layers help confine modes to the LiNbO₃ region. The waveguide has a trapezoidal cross-section and is etched into the LiNbO₃ layer.

2.3.2 Fiber optics

The LNO has required that this project use 1550 nm telecom wavelength light and single-mode SMF-28 optical fibers. This allows for a more cost-effective setup, since telecom components are less expensive, and the laboratory already has plenty of SMF-28 fibers and photodiodes that measure 1550 nm wavelength light.

2.3.3 Size constraints

The entire alignment setup must fit on an optical table working space in the LNO, which is 80 cm × 50 cm. This is the space that the LNO gave me to work in, and it is typically the space given to a single scientist to conduct their experiments.

2.4 Design approach

2.4.1 Overview

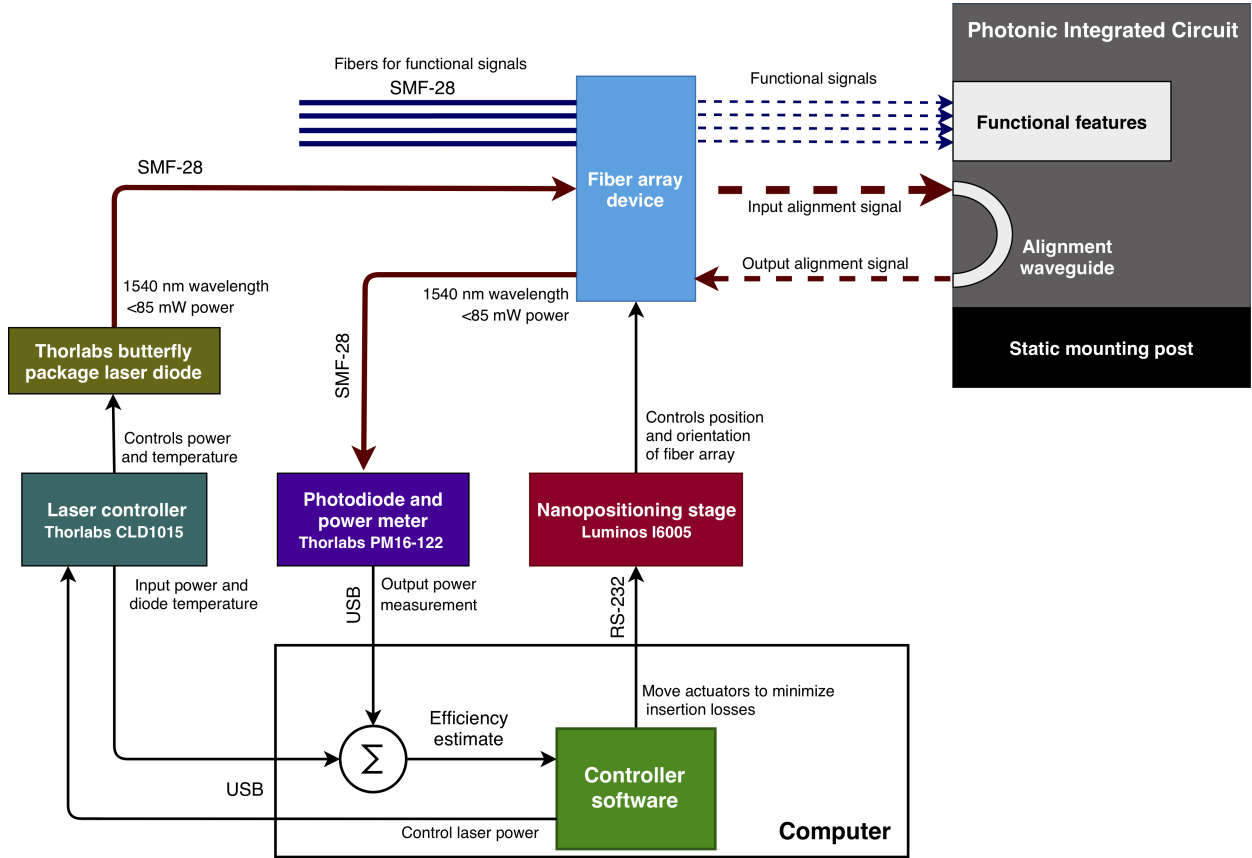


Figure 2.2: System diagram

The system design as depicted in Figure 2.2 is a feedback loop designed to align an array of fibers to an array of PIC waveguides in edge coupling. A laser diode injects a mode along a SMF-28 fiber in a linear fiber array device. The orientation of the fiber array device is controlled by a 6-axis nanopositioning stage. The input fiber is designed to couple with one end of a U-shaped waveguide on a static LiNbO₃ PIC. The width of the U shape is the same as the spacing as fibers in the array, so when the fiber array is aligned properly with the PIC waveguide, two adjacent fibers will couple with the PIC waveguide simultaneously. The fiber adjacent to the input signal fiber will then carry the coupled signal to a photodiode and power meter. Controller software running on a desktop computer can then use the level of coupling and spatial information from the nanopositioning stage to determine how to improve the coupling efficiency of the system.

2.4.2 Edge coupling

An edge coupling configuration was chosen for its higher maximum coupling efficiency

compared to that of grating coupling. While grating coupling allows for looser misalignment tolerances, the insertion losses that it effects are too high to reliably perform the quantum optics experiments that the LNO is pursuing.

2.4.3 PIC architecture

Any PIC designed to work with this project's process must have some functional feature that allows for a measurement of coupling efficiency. The input mode from an optical fiber onto the PIC must also return from the PIC to be measured. A simple way of getting light off the PIC is to couple a mode from a PIC waveguide to an optical fiber, which is physically symmetric to the insertion coupling. One simple example of PIC architecture that allows for measurement of coupling efficiency as well as access to functional components on the PIC is depicted in Figure 2.3.

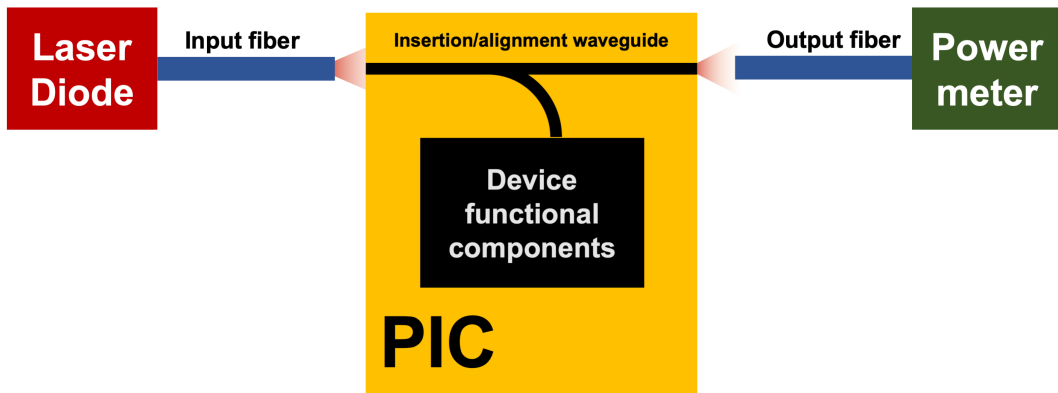


Figure 2.3: Schematic of a PIC with a splitting waveguide for measuring coupling

This architecture, while simple, is not feasible. The coupling efficiency would then have to be extrapolated from the total power loss over two coupling points and a waveguide split. Since maximum coupling efficiency in production devices is a primary concern of this project, designing signal losses into the alignment system defeats the purpose of the process. Also, the input fiber and output fiber would have to be perfectly aligned with each other in order to measure coupling. Assuming the input and output fibers are aligned, though, this architecture allows for alignment in all degrees of translation and two degrees of rotation. Rotation about the axis of the fibers is unconstrained for non-polarized light.

An approach considered, depicted in Figure 2.4, was to use a separate fiber in a fiber array device so that the alignment and functional signals could be separated. This architecture solves the issue of signal loss due to the signal splitter, but it still relies on perfect alignment of the alignment fibers before the PIC is in place. Moreover, there is no guarantee that the functional insertion fiber will be properly aligned when the alignment insertion fiber is aligned with the alignment waveguide since the transmission to the power meter will not change as the PIC rotates about the axis of its alignment waveguide.

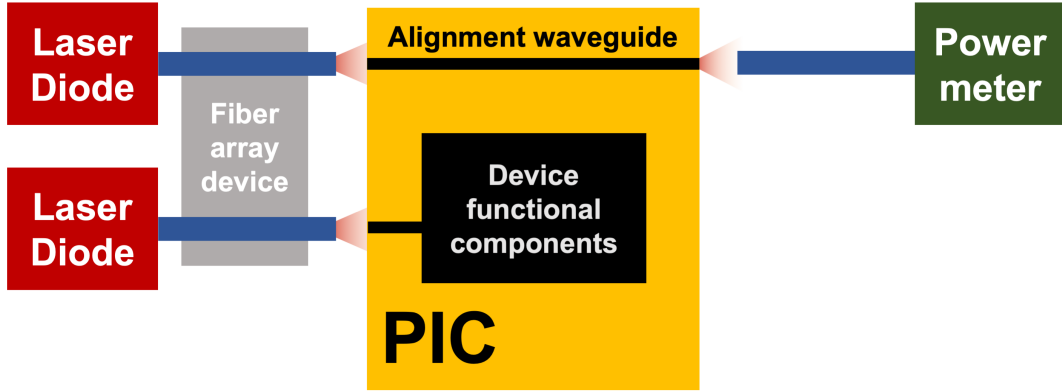


Figure 2.4: Potential PIC architecture for coupling with a single fiber in a fiber array

To correct for the rotation issue, two parallel alignment waveguides could be included on the PIC as depicted in Figure 2.5. With two power meters and two independent light sources, one could properly align the PIC with respect to an arbitrarily large fiber array with two of the fibers in the array dedicated to alignment. This architecture is undesirable because it requires multiple power meters just for alignment, and it is unfeasible because it still relies on perfect alignment of the alignment-dedicated fibers before the PIC is involved in the setup.

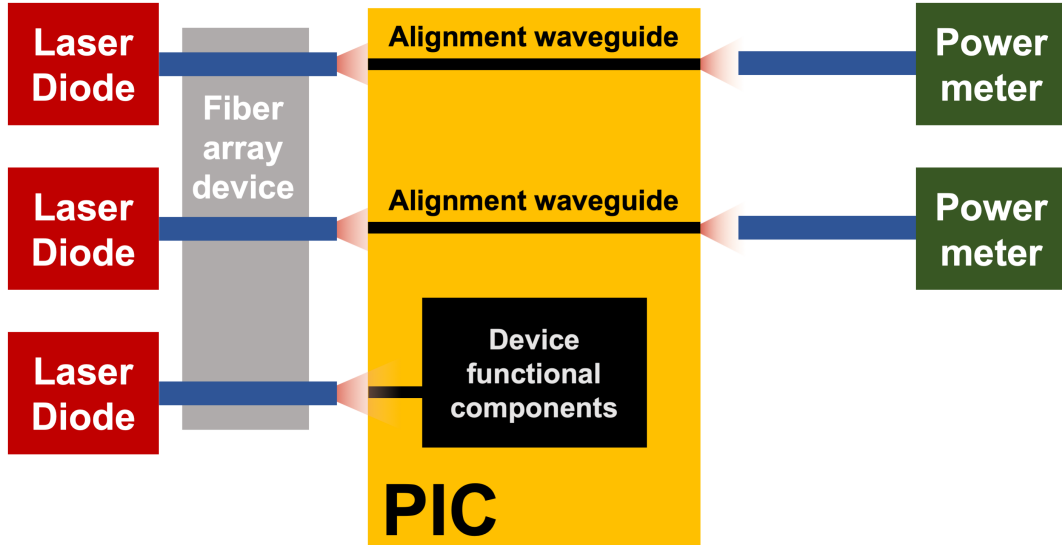


Figure 2.5: Potential PIC architecture for coupling with arbitrarily many fibers in a fiber array

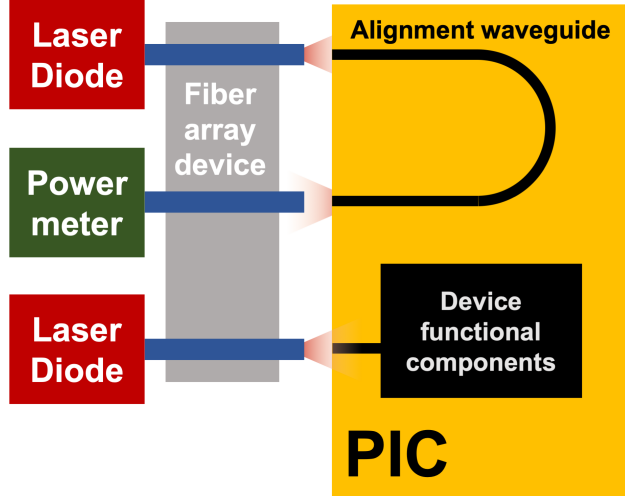


Figure 2.6: PIC architecture for coupling with arbitrarily many fibers in an array using a single light source and power meter

A U-shaped waveguide like the one depicted in Figure 2.6 allows for optimization of alignment in all six degrees of freedom for arbitrarily-many fibers in a linear array in edge coupling while only using a single light source and single power meter. The fiber array device constrains the alignment fibers to be parallel and predictably spaced. The power loss per facet would be half of the measured power loss from the light source to the power meter. This U-shaped waveguide design is the design that has been fabricated for the prototyping purposes of this project.

2.5 Component selection

2.5.1 Interposer

The PIC architecture is designed for a fiber array device. To minimize MFD mismatch between the optical fibers and the PIC waveguides, we utilized a LioniX TriPleX fiber array device with an integrated Si_3N_4 interposer PIC that contains waveguides with MFDs similar to those of the target PIC waveguides. The interposer, described in Figure 2.7, has two loops that allow for testing and measurement of fiber-to-waveguide losses.

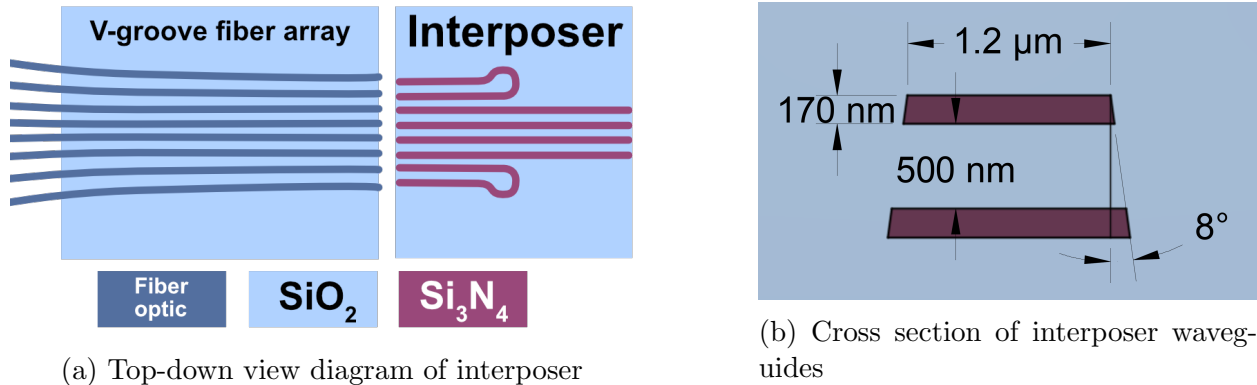


Figure 2.7: Schematic of LioniX fiber array device with interposer

2.5.2 Nanopositioning stage

The technical specifications restricting the choice of device actuator are the alignment precision and automation specifications. Manual micrometer stages can have gradations as small as $0.5 \mu\text{m}$, but they have significant backlash and require a human operator.



Figure 2.8: Example of a XYZ manual micrometer stage [10]

The LNO provided this project with a Luminos I6000 nanopositioning stage, which has a linear motion resolution of 4 nm and backlash of 20 nm. The stage has six stepper motors that actuate a flexure stage, allowing for positioning and orienting of fibers or PICs. The full specifications of the stage can be found in Appendix A. The stepper motors can be controlled using the Zaber Binary protocol in a number of modern programming languages.

Because the center of rotation of the stage is in front of and above the mounting plate surface, a clamping device, shown in Figure 2.9, was designed for holding the interposer's facets near the center of rotation of the stage. Besides being mathematically convenient, placing the interposer near the center of the stage's rotation prevents translation error from rotational motion from becoming larger than the small 0.5 mm movement range of the stage along its horizontal and vertical axes.

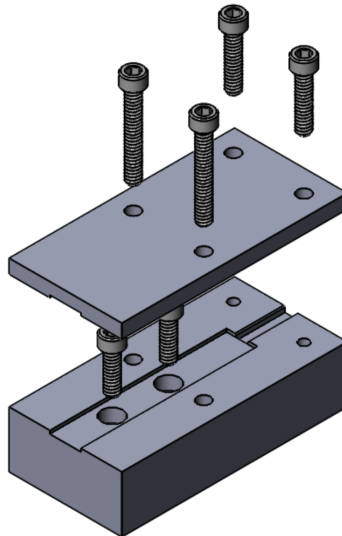


Figure 2.9: Exploded view of interposer clamp

Full engineering drawings can be found in Appendix B. The clamp is designed to be machined from steel, which is very stiff and has a low thermal expansion coefficient among metals. For prototyping purposes, the clamp was 3D-printed.

2.5.3 Photodiode and power meter

The LNO has a number of Thorlabs PM100 series power meters and S150 series fiber photodiodes. For the purposes of the project, a Thorlabs PM16-122 compact USB combined photodiode and power meter was a good fit because of its ability to precisely measure 1550 nm radiation through an optical fiber and interface with computer programs. Its small size and lack of a bulky integrated display like a Thorlabs PM100A power meter means that it will take up less space on the constrained laboratory table. The specifications for the PM16-122 can be found in Appendix C.

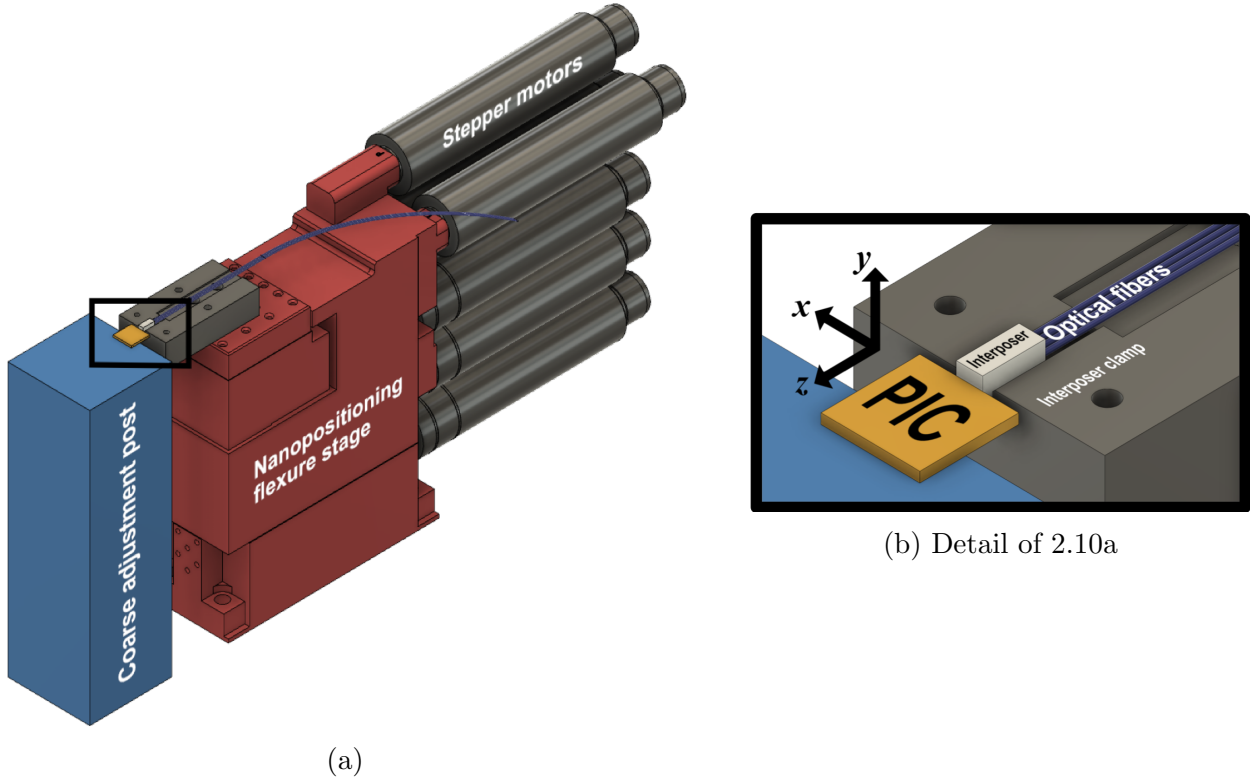


Figure 2.10: Layout of clamp and interposer on nanopositioning stage. Note the left-handed coordinate system of the stage.

2.5.4 Light source and controller

The laser diode that supplies light to the system has 85 mW peak power and a center wavelength of 1540 nm with a bandwidth of 30 nm. The laser diode is controlled by a Thorlabs CLD1015 laser controller.

2.6 Simulation

Simulations were employed in order to characterize the sensitivity of coupling to misalignment. These simulations informed the resolution of our fine-grain searches when programming alignment algorithms and verified that it would be possible to achieve first light coupling.

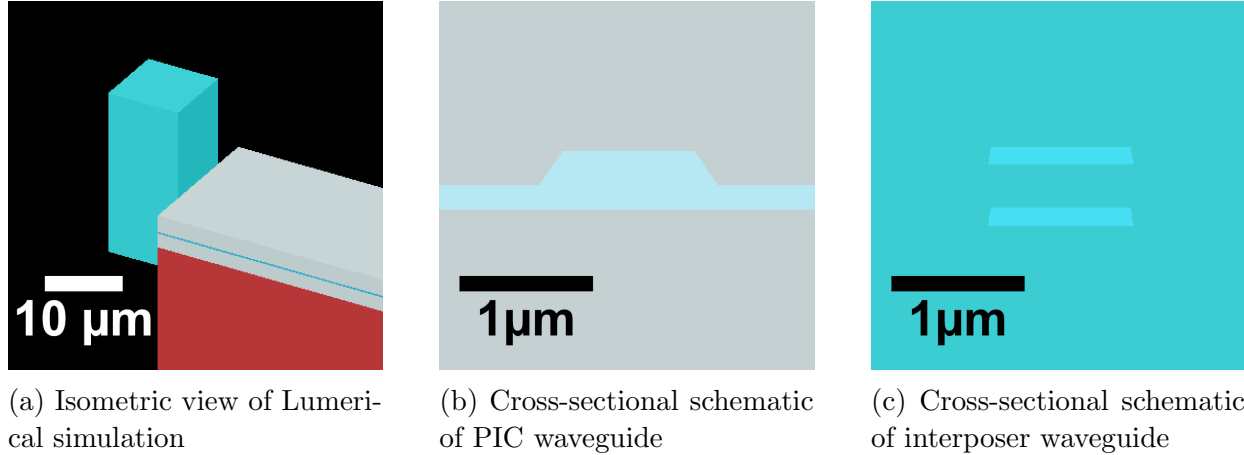


Figure 2.11: Screenshots from Lumerical simulation

The script that generated the geometry used can be found in Appendix D. All simulations attempt to describe the coupling of a single PIC waveguide to a single interposer waveguide. Figure 2.11a is a schematic of the simulation geometry. The cyan block on the left represents a single Si_3N_4 interposer waveguide and its cladding glass. The multicolor sandwich on the right is the PIC, with the silicon handle wafer in red, the cladding oxide in grey, and the LiNbO_3 layer in cyan. The cross sections of the two types of waveguide are depicted in Figures 2.11b and 2.11c.

2.6.1 2D FDE

To rapidly gain an understanding of the misalignment tolerance of the system, an eigenmode solver was employed to calculate the overlap of the fundamental modes of the PIC and interposer waveguides. Lumerical's Finite Difference Eigenmode (FDE) solver solves Maxwell's equations on a two-dimensional mesh of a cross section of a waveguide [11]. The solver returns the effective index and mode profiles of waveguide modes. The solver is based on Zhu and Brown's solver [12], with proprietary modifications.

By shifting the mode profiles with respect to each other, the solver can calculate the coupling efficiency change as the PIC and interposer shift laterally with respect to each other. This simulation, being two-dimensional, assumes zero axial displacement, as depicted in Figure 2.11a. The simulation suggested that the maximum power coupling of the two waveguides when optimally aligned is -1.36 dB . The coupling efficiency drop-off with misalignment is rather severe, with -15 dB loss with $1 \mu\text{m}$ of misalignment and -25 dB with $2 \mu\text{m}$ of misalignment. The simulation results are roughly symmetric with respect to verti-

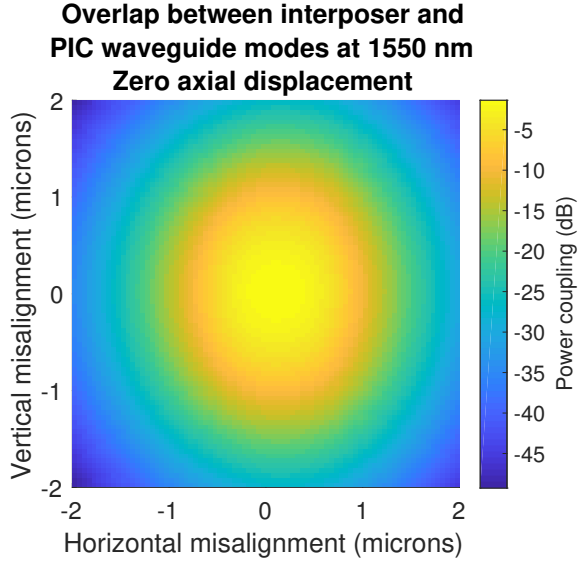


Figure 2.12: Results of FDE simulation

cal and horizontal misalignment, with the coupling efficiency decreasing less severely with vertical misalignment.

According to this simulation, we could expect as much as -50 dB attenuation during the alignment process until both coupling points are within $2\ \mu\text{m}$ of the optimal coupling point in lateral misalignment.

2.6.2 2.5D varFDTD

The FDE simulation described the power overlap of two modes as they shifted with respect for each other but did not account for axial displacement. During the alignment process, the two components start with a few microns of space between them, so a simulation that does not reflect that might be misleading and not quite as informative for the early stages of the alignment process.

Lumerical's Variational Finite Difference Time Domain (varFDTD) solver is a time-dependent solver that solves Maxwell's equations in time in three dimensions by collapsing a three-dimensional set of effective indices into a two-dimensional set by averaging refractive indices along one axis [13]. For this reason, the simulation is considered 2.5D. The approximation in this particular simulation reduced computation time by two orders of magnitude compared to a full 3D simulation. The disadvantages of a 2.5D solver are the loss of accuracy and being constrained to two dimensions for displacements. The two-dimensional constraint was overcome by rotating the geometry of the entire simulation 90° and simulating vertical and horizontal misalignment separately. Power transmission was measured by a power monitor along the PIC waveguide $50\ \mu\text{m}$ away from the facet.

The varFDTD simulations paint a much more promising picture for the possibility of achieving weak coupling. While the maximum coupling efficiency predicted by the varFDTD simulations is the same as that predicted by the FDE simulations, the drop-off of coupling efficiency with both lateral and axial displacement is much less severe. The horizontal

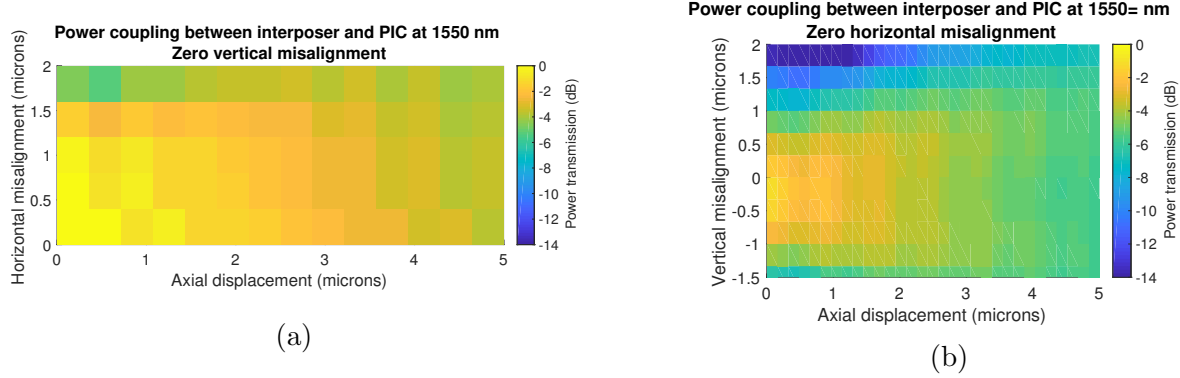


Figure 2.13: Results of varFDTD simulations in two planes

misalignment simulation (Figure 2.13a) suggests that a coupling efficiency as high as -5 dB can be expected with $2\text{ }\mu\text{m}$ of horizontal misalignment and $5\text{ }\mu\text{m}$ of distance between facets along the z -axis. The vertical misalignment simulation does not suggest quite as efficient coupling at similar distances and misalignments, but it does suggest that the sensitivity of coupling efficiency to misalignment decreases as axial displacement increases. This is important because it suggests that first light coupling might be easier to achieve when the components have a few microns of space between them.

It was expected that the horizontal displacement simulation would suggest higher levels of power transmission. In that simulation, effective indices had been averaged along the vertical direction (y -axis), and so the two-layer geometry of the interposer waveguide had been flattened into a single layer. In the vertical misalignment simulation, effective indices were averaged horizontally (x -axis), and thus the two-layer structure was preserved. The difference in mode profile between the two-layer interposer waveguide and the single-layer PIC waveguide contributed to the decreased coupling efficiency in the vertical misalignment simulation.

2.7 Control software

The control software is designed to achieve and maintain alignment. To achieve these functions, the software must be able to interface with the hardware components. Python was chosen as the programming language for this project to best meet these requirements. There are open-source libraries for interfacing with scientific equipment like the nanopositioning stage and power meters, as well as libraries for scientific computing, graphical plotting, and computer vision. Python is also a easy language for rapidly prototyping software because of its readable syntax and robust standard libraries. MATLAB shares many of these useful characteristics, but its closed-source nature and expensive licensing made it inconvenient for long-term use.

The alignment algorithm has four steps:

1. Find first light
2. Optimize in translation
3. Optimize in rotation
4. Maintain alignment for fastening

2.7.1 First light

The user will manually align the interposer and PIC waveguides as well as possible. With a few microns of space between the interposer and PIC along the z -axis, the software will first perform a coarse two-dimensional translation sweep in the xy -plane, as depicted in Figure 2.14, while taking readings from the power meter to find a local maximum of coupling efficiency. The step size of the sweep should be approximately 1 μm given the results of the simulation.

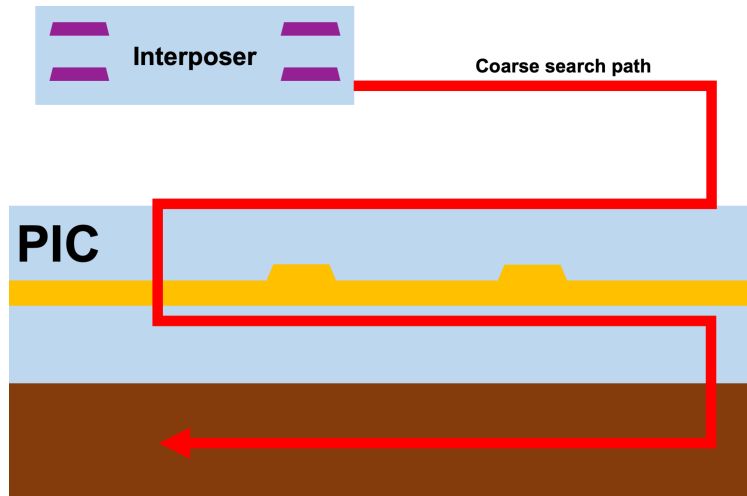


Figure 2.14: View along z -axis of waveguide cross sections and first light search path

2.7.2 Translation optimization

Once weak coupling has been achieved, the interposer can be moved closer to the PIC along the z -axis. With each approach step, smaller xy -plane sweeps with finer resolutions should be performed to update the x, y -coordinates of the coupling efficiency maximum. To prevent the components from crashing, computer vision software can be integrated with a high-power optical microscope to determine when the components are about to collide. If a lensed fiber is used, then coupling efficiency will reach a maximum with a few microns of space between the components, and computer vision software will not be necessary.

2.7.3 Rotation optimization

When the PIC-interposer alignment is transitionally-optimized, gradient ascent in the three rotational degrees of freedom can be used to gradually orient the stage into orientations with higher and higher coupling efficiencies. Every few rotations, an xy -plane sweep must be performed in order to correct for misalignment in translation caused by the rotation of the stage.

2.7.4 Maintain alignment

Once optimal alignment in all six degrees of freedom is achieved, the stage can maintain alignment by perturbing its location and orientation slightly and checking if the coupling efficiency increases substantially during perturbations. The gradient of the coupling efficiency with respect to translation and rotation can be estimated using two measurements in each direction in each degree of freedom, for a total of 2^6 readings.

2.8 Packaging

A UV-curing adhesive is used to fasten the interposer to the PIC. This method allows us to replace the air between the interposer and PIC with an index-matched medium and realign after the adhesive is deposited. This method is also simpler than using a laser-welded metal ferrule and requires no enclosure.

Chapter 3

Build

3.1 Software

3.1.1 Stage control module

A Python module for controlling the nanopositioning stage's actuators was developed in order to add a layer of abstraction and facilitate search algorithm implementation. The stage control module allows the user to connect to a Luminos I6000 stage via its included RS-232 serial connection. The module includes basic functionality for changing its orientation and recalibrating the stage. Code for the module can be found in Appendix E.

Zaber Binary protocol

All actuation functionality is programmed through the Zaber Binary protocol [14]. The protocol uses a message/reply paradigm. Messages are six-byte instructions:

- Byte 1: Device number
- Byte 2: Command number
- Bytes 3-6: Data

The device number tells the stage which actuator to move. The command number indicates the type of instruction. The last four bytes are data that is relevant to the command number. For example, the command to move the z -actuator to absolute step 3100 would be given by

Device number	Command number	Data
1	20	3100

When the stage completes an instruction, is tracking a move, or encounters an error, it generates a reply and places it in a buffer queue. Reply structure is fundamentally identical to that of message structure. Replies must be actively read from the buffer. The stage module waits for instructions to complete before returning to the caller program by polling the stage until the desired reply is received.

3.1.2 Taking measurements

The Virtual Instrument Software Architecture (VISA) is an API that allows computers to interface with scientific instruments. Pierre Clade's ThorlabsPM100 Python package [15] uses a Python implementation of VISA to interface with Thorlabs power meters, including the PM16-122 that we use. We have implemented functions that allow the stage to record the power meter value at all points in a one- or two-dimensional sample space. Functions have also been implemented to automate the process of restricting the search space to the regions near the local maximum of the coupling function.

3.2 Hardware

The laboratory setup, pictured in Figure 3.1, includes all the components described in the design as well as a few additions in order to facilitate speedy coupling. A prototype of the interposer clamp has been 3D-printed out of PLA and mounted on the micrometer stage. Translation at the facets due to 1 degree of rotation measures less than $30\text{ }\mu\text{m}$. The PIC has been bonded with adhesive to a glass slide and fixed to a micrometer stage. The micrometer stage is imprecise and has significant coupling between its axes, but it allows for coarse adjustments of the PIC's position. An high-power optical microscope has been mounted above the table to aid alignment by eye before starting the automated alignment program. A second low-power microscope (not pictured in Figure 3.1) has been mounted to look along the x -axis and aid in y -axis alignment.

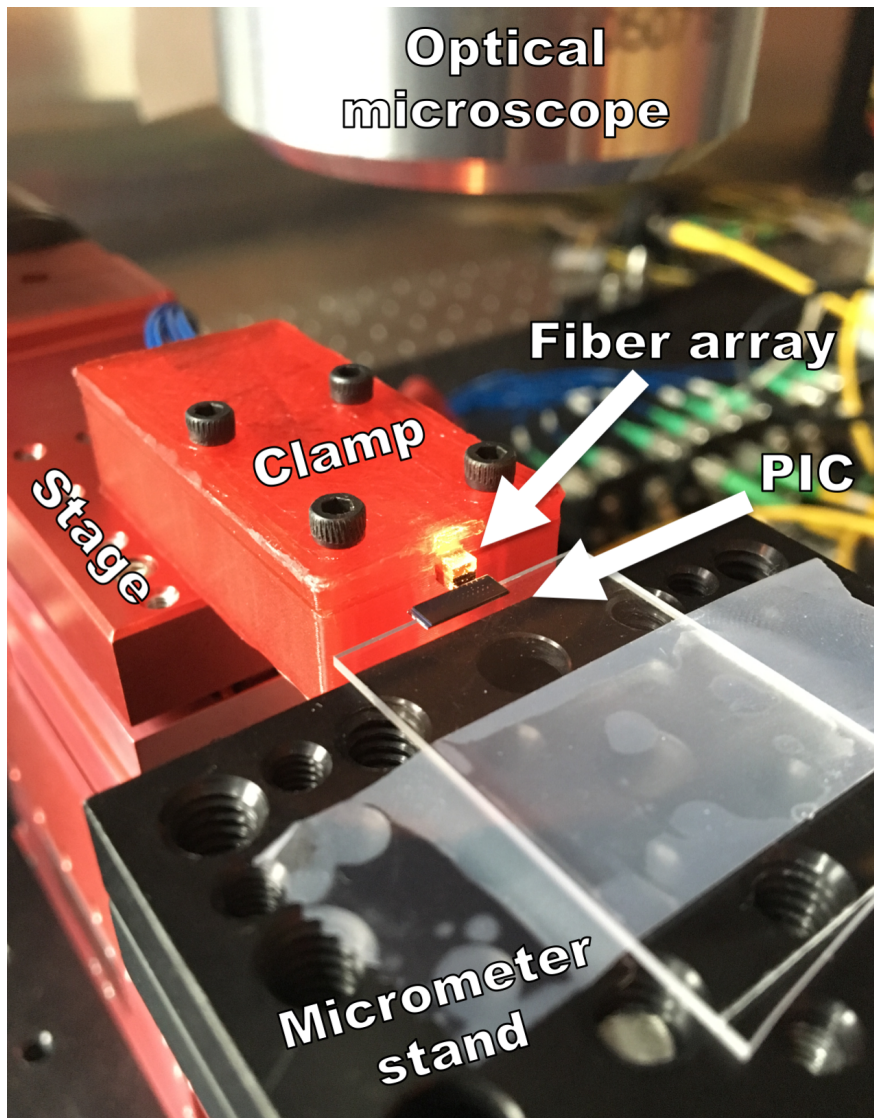


Figure 3.1: Photograph of an interposer-PIC coupling setup

A simpler setup, which has been used for testing the automated alignment program, aimed to achieve interposer-to-fiber coupling, first with a planar polished facet fiber and then with a lensed facet fiber. This setup utilized an off-the-shelf fiber holder. A close-up view of the interposer-to-fiber coupling setup is shown in Figure ??.

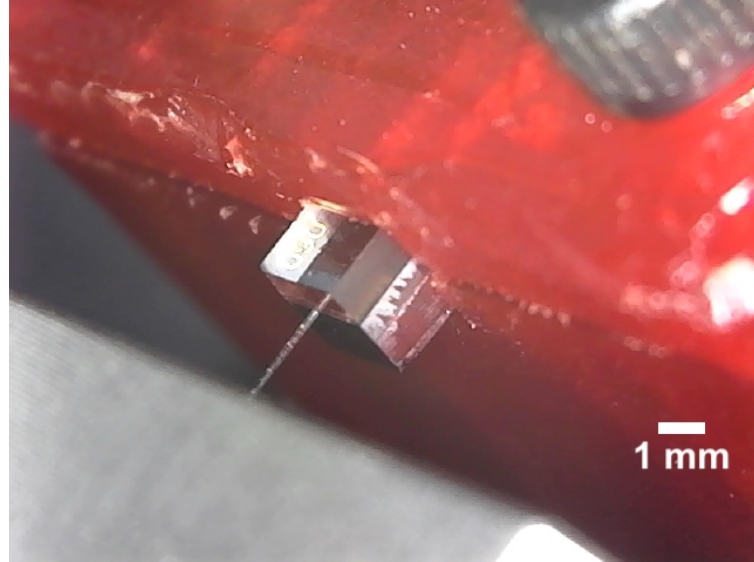


Figure 3.2: Micrograph of lensed fiber coupled to interposer

The PIC, shown in Figure 3.3, was designed and fabricated by CJ Xin, and contains U-shaped waveguides with various waveguide widths and ring resonators on half of the waveguides. Ring resonators allow for measurements of changes in wavelength of the input signal, something that is not directly relevant to this project.

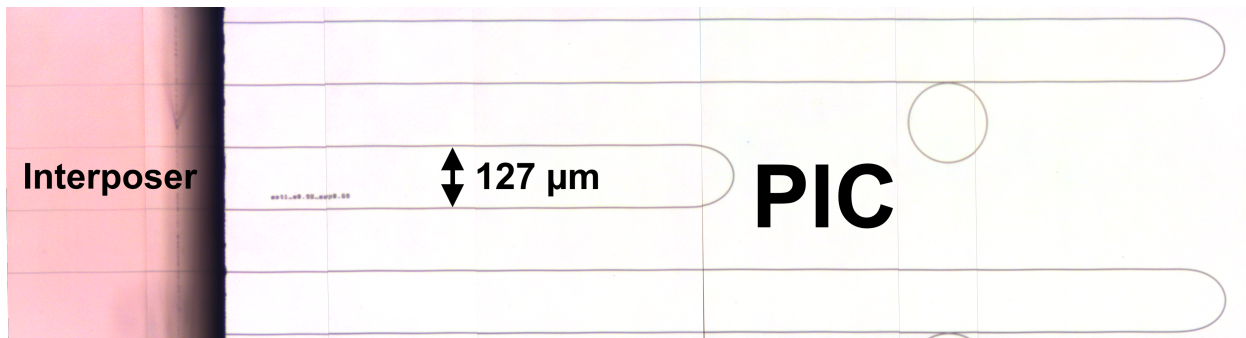


Figure 3.3: Composite false-color micrograph of PIC showing waveguide design

Chapter 4

Measurement

4.1 Interposer-to-fiber coupling

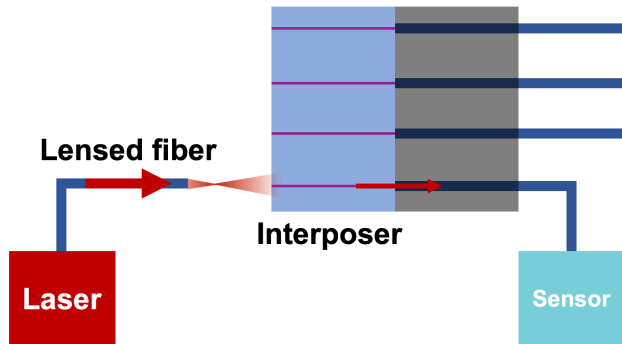


Figure 4.1: Schematic of fiber-to-interposer coupling with a lensed fiber

The first attempts at coupling were performed using a single-point interposer-to-fiber configuration like the one depicted in Figure 4.1. The purpose of this configuration was to ensure that the process would work for the simplest PIC-to-fiber coupling scenario before attempting to couple to two waveguides at the same time. An optical fiber has a large MFD, so it is possible to find first light with a coarse step size.

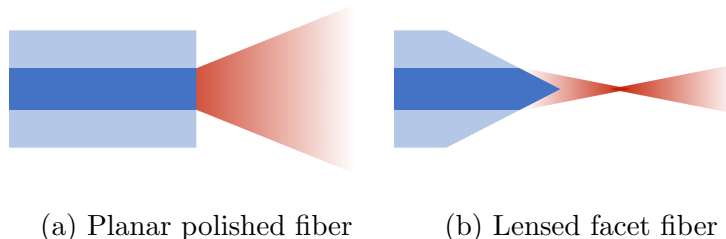


Figure 4.2: The two kinds of fibers employed for attempting interposer-to-fiber coupling

Two different kinds of fibers, depicted in Figure 4.2, were employed. Planar polished fibers have end facets that are flat and perpendicular to propagation direction of the beam.

The MFD of the light from planar polished fiber increases as it moves away from the fiber. Lensed fibers, on the other hand, have pointed tips that focus the light into a Gaussian beam. The beam has a small waist that is better matched to the small MFD of a PIC waveguide.

In under ten successive xy -plane scans, it is possible to reduce the search space size to 2 μm per side and the spatial sampling resolution to 0.15 μm with both planar polished and lensed facet fibers. Figure 4.3 shows the data that the software analyzes in order to determine the xy -position of optimal alignment. The plots show coarse measurements taken with a few dozen microns of axial displacement between the fiber and interposer.

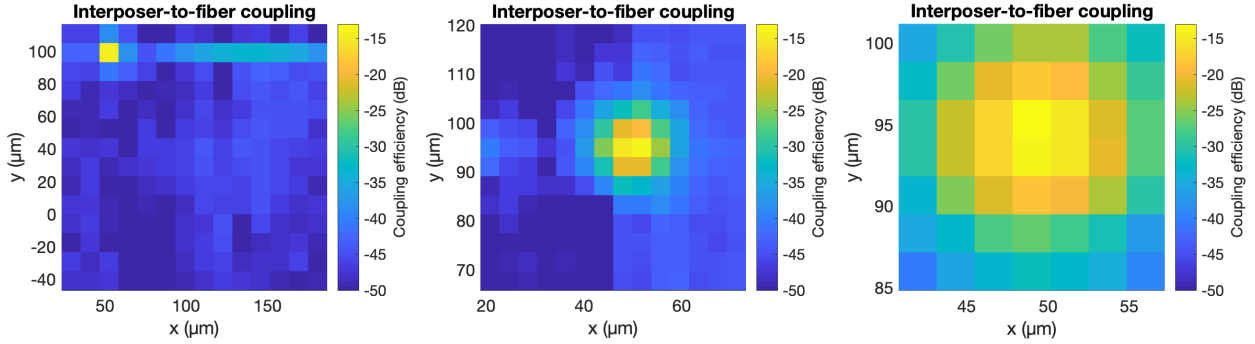


Figure 4.3: Finding the local maximum of coupling efficiency between a lensed facet fiber and the interposer on the xy -plane with a large z -displacement. Note the decrease in search space size going from left to right.

Once the xy -center of coupling efficiency is found, the software can gradually decrease axial displacement until the user stops the process or a maximum in the coupling signal is achieved.

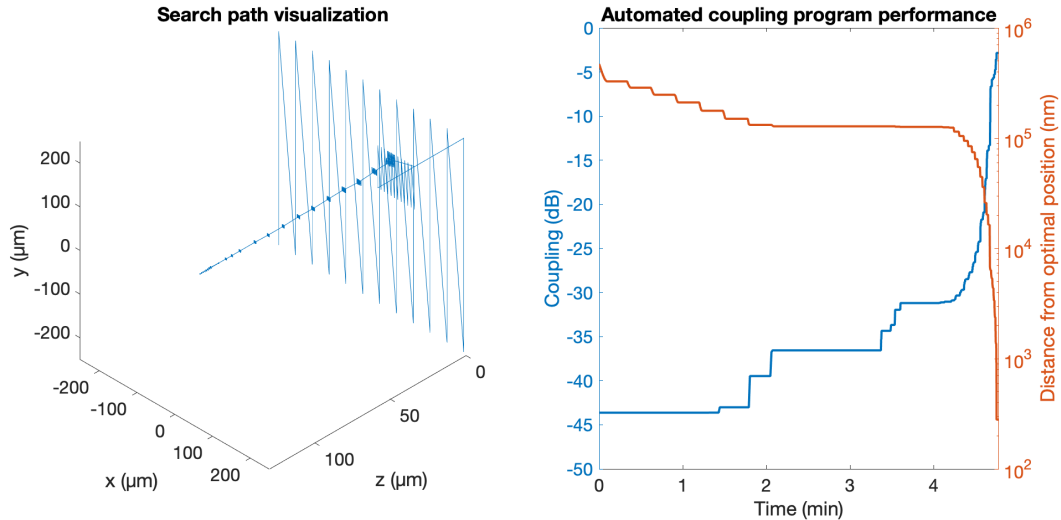


Figure 4.4: Left: A visualization of the search path of the interposer head. Right: The evolution of coupling efficiency between the lensed fiber and the interposer over time.

Figure 4.4 depicts a measurements from a trial of the automated alignment algorithm performed between a lensed facet fiber and the interposer. The software decreases the search

space size on the xy -plane exponentially first, then closes the axial distance between the fiber and the interposer. After each step along the z -axis, the interposer head is swept along the xy -plane to correct for any lateral misalignment that might have resulted from the axial translation. The axial distance that the interposer is moved with each step is inversely proportional to the gradient of the logarithm of the coupling efficiency with respect to axial displacement. Figure 4.5 makes it clear why this modified gradient ascent might be advantageous for lensed fibers.

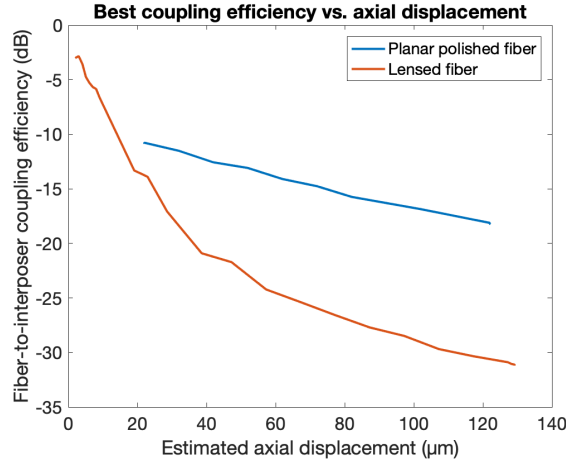


Figure 4.5: Measured best coupling efficiency while moving interposer closer to fibers after optimizing alignment in xy -plane

When the lensed fiber is far from the interposer, large axial steps can be taken because there is low risk of crashing. A large distance from the interposer can be inferred by the shallow slope of the coupling versus axial displacement graph. Likewise, the gradient of coupling efficiency spikes when the lensed fiber is close to crashing, so the software uses that fact to decrease step size.

To avoid crashing lensed fibers, the algorithm takes small enough steps that the interposer head can be moved past the waist of the lensed fiber's Gaussian beam, which lowers the coupling efficiency, without crashing the fiber into the interposer. For planar polished fibers, coupling efficiency does not have a convex maximum. Instead, coupling efficiency will increase until the fiber crashes.

The automated coupling trials were able to achieve a best coupling efficiency of -2.8 dB and identified the optimal coupling position within 300 nm. The process lasted approximately five minutes, with roughly four minutes of that time spent on large, coarse sweeps searching for first light. With an optimized search algorithm, this level of coupling could likely be achieved in under a minute.

4.2 Interposer-to-PIC coupling

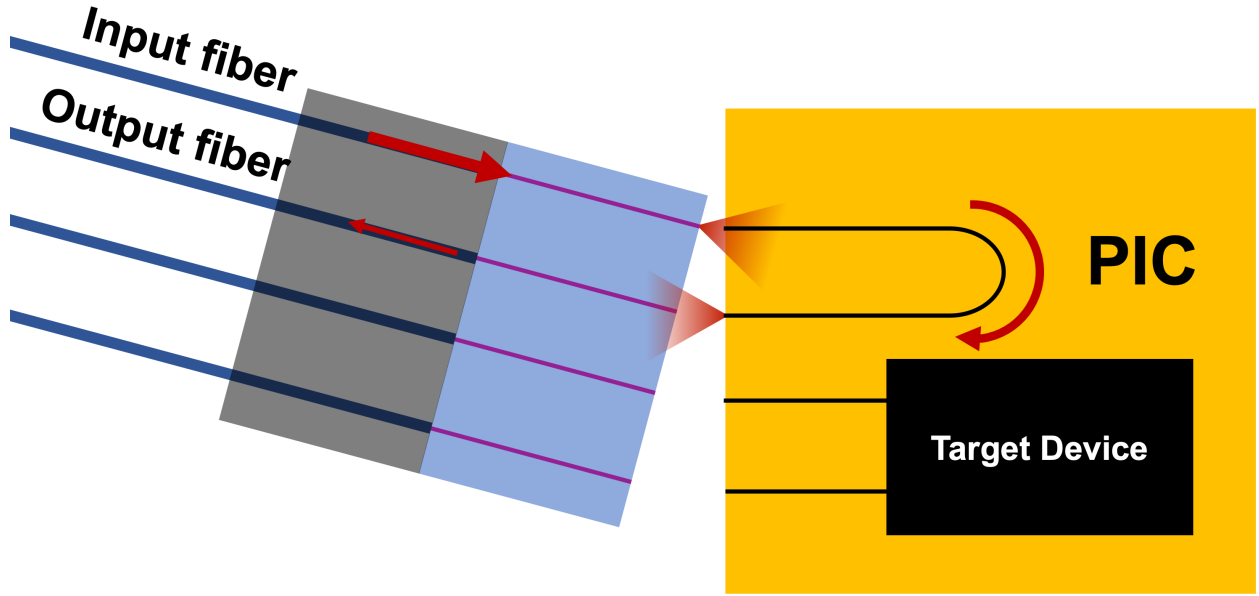


Figure 4.6: Schematic of two-point interposer-to-PIC coupling with U-shaped waveguide architecture.

Achieving multi-point interposer-to-PIC coupling has proven to be much more difficult than achieving interposer-to-fiber coupling. This is because coupling needs to be achieved simultaneously on two facets, and until very precise alignment is achieved, the power transmitted through the alignment waveguide depicted in Figure 4.6 less than background noise.

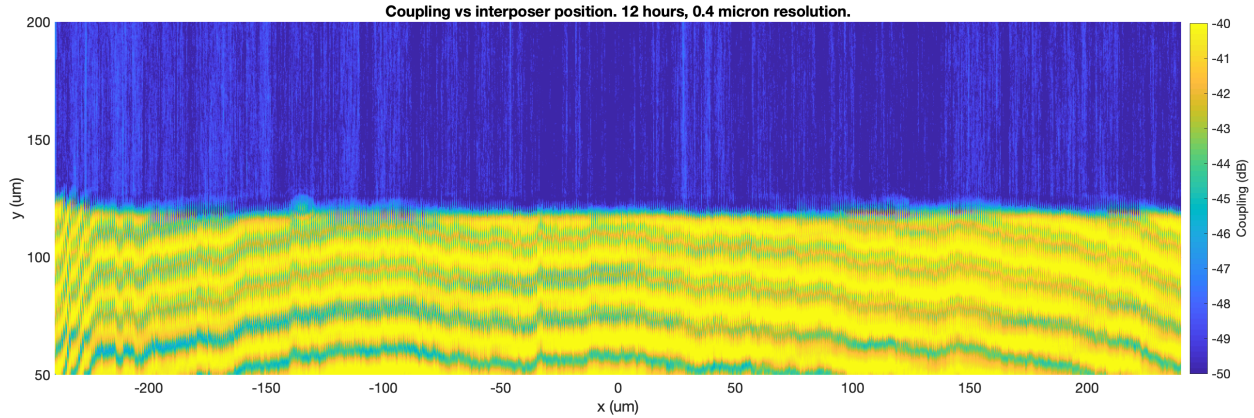


Figure 4.7: $480 \mu\text{m} \times 150 \mu\text{m}$ sweep of interposer on xy -plane

Based on insights from simulation, a 12-hour scan with $0.4 \mu\text{m}$ step size was performed on the xy -plane. This scan, shown in Figure 4.7, images the top edge of the PIC. The low-transmission region on top represents y -coordinates at which the interposer was above the top of the interposer and thus was emitting a signal into open air. The lower, banded region with higher transmission represents y -coordinates at which the interposer waveguide

was emitting light into the side of the PIC. This light bounced off the side of the PIC and was received by the interposer waveguide connected to output fiber.

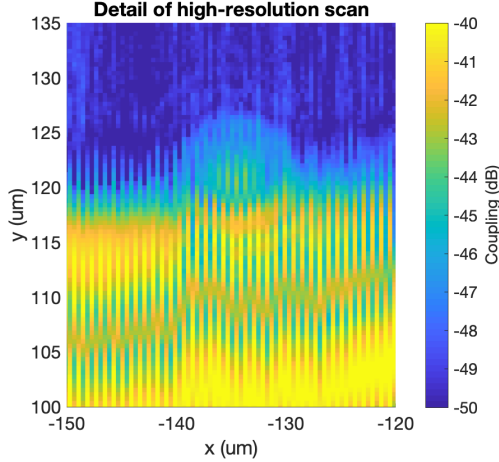


Figure 4.8: Detail of Figure 4.7 with a circular region that could be evidence of coupling.

It is unclear whether any significant coupling through the U-shaped waveguide was achieved. There is one region at $x = -135 \mu\text{m}$ and $y = 122 \mu\text{m}$ that is detailed in Figure 4.8 with a circular pattern. The radial symmetry of the region and its location on the top of the chip suggests that it could be evidence of true coupling. However, coupling would be exceptionally low (-44 dB). It is likely that the rotational misalignment of the fiber array was large enough to prevent any measurable coupling.

4.2.1 Path dependence

One issue that has become clear is that the scans of the PIC facet give results that are dependent on the path that the interposer takes. Figure 4.9 demonstrates how the banding pattern of the reflections off the side of the PIC changes depending on whether the interposer head scans points with long movements along the y -axis or along the x -axis.

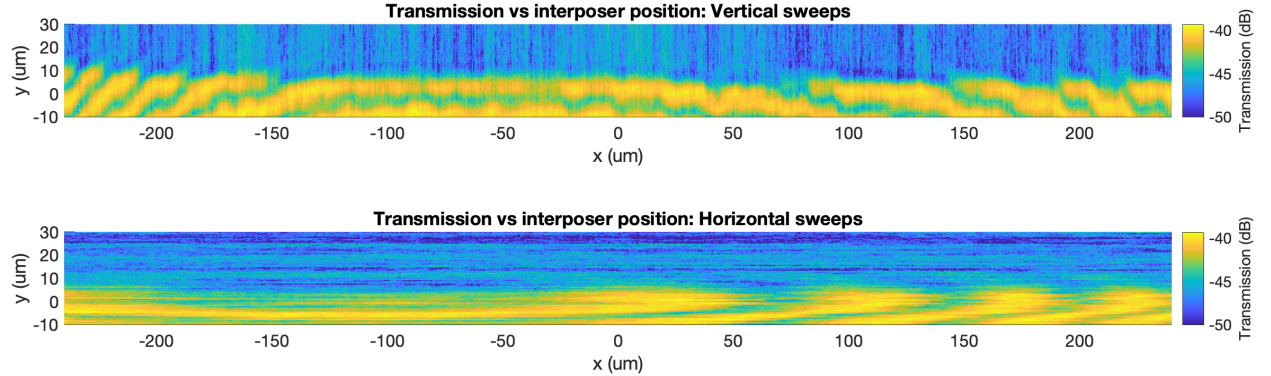


Figure 4.9: Difference in reflection pattern recorded depending on direction of zig-zags

The banding pattern on the side of the PIC appears to be perpendicular to the motion of

the interposer head, and the banding pattern in the air above the PIC appears to be parallel to its motion.

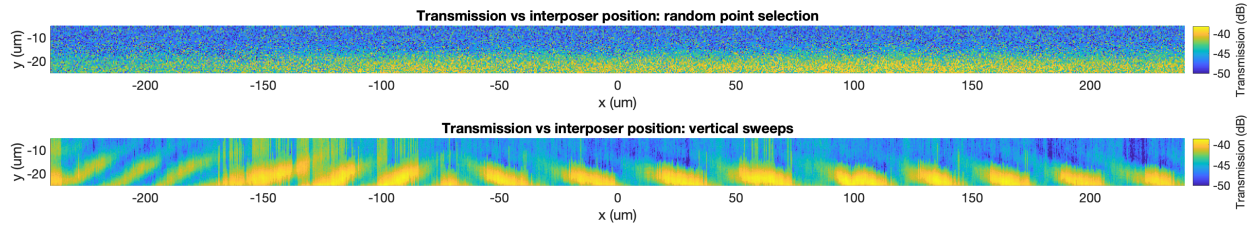


Figure 4.10: Demonstration of the elimination of banding pattern due to random path

Performing scans by randomly selecting points in the sample space until the space is exhausted, as demonstrated in Figure 4.10, eliminates the banding patterns, but seems to decrease the sharpness of the scans. Besides decreasing apparent resolution, the random point selection scans take three to four times as long as the zig-zag scans because of the increased travel distance between points. Perhaps a Hilbert curve search path, or some other space-filling curve, would be a good compromise between minimizing search distance and randomizing the direction of movements between points in order to reduce banding artifacts.

Chapter 5

Conclusion

5.1 Evaluation

Specification	Results
Keep fabrication process on Harvard's campus	All custom components fabricated on-campus
Achieve alignment in under 16 hours	Alignment achieved in 5 minutes
Achieve alignment within $\pm 1.2 \mu\text{m}$ of optimal	Alignment achieved within 300 nm of optimal
Maintain $\pm 1.2 \mu\text{m}$ alignment tolerance over 10 °C variation	Mechanical fastening not attempted

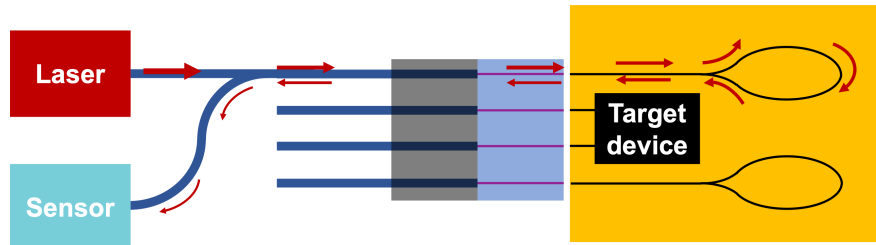
Single-point optical coupling between an optical fiber and interposer PIC was achieved via an automated alignment process that achieved alignment within 300 nm of optimal within 5 minutes. The maximum coupling efficiency achieved was -2.8 dB , which approaches the -1 dB coupling efficiency expected a PIC with optimized waveguide geometry[4], something the test PIC did not have.

Because of the COVID-19 pandemic that caused the evacuation of Harvard's campus and shutdown of laboratories, experiments with fastening the optical fiber to the interposer were not attempted.

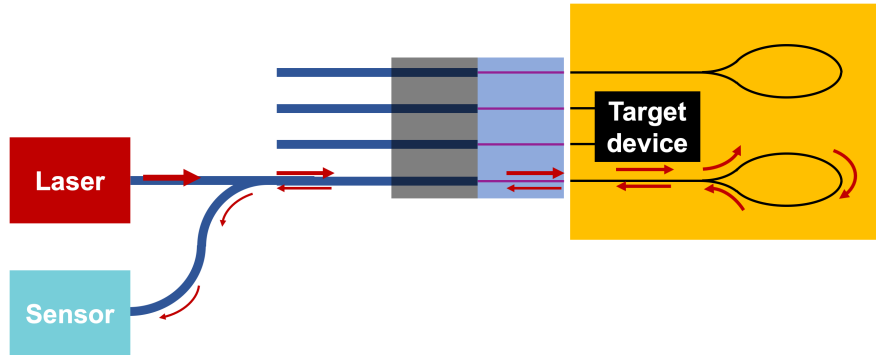
5.2 Next steps

The ease with which single-point coupling was achieved and the elusiveness of two-point coupling suggest that a different approach for aligning a linear fiber array with a linear array of PIC waveguides. One possibility is to perform single-point coupling in two locations, and use the positional information to determine the line on which all waveguides lie.

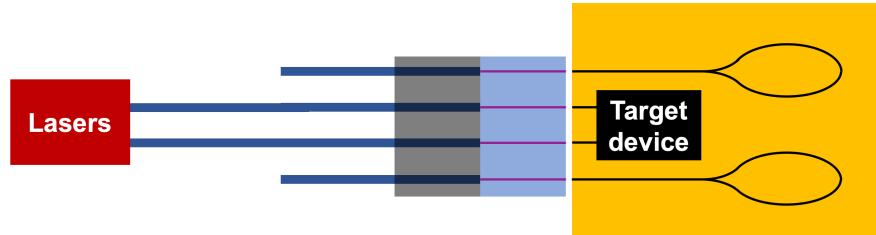
Figure 5.1 describes the procedure in more detail. The two outermost fibers on a linear fiber array are aligned to reflecting waveguides on a PIC (Figures 5.1a and 5.1b). These reflecting waveguides are the outermost waveguides in a linear array of PIC waveguides with pitch matching that of the fiber array. The interior waveguides on the PIC lead to the structures that perform the desired functionality of the device. With analysis of the positions at which single-point coupling is maximized between the fibers and the reflecting



(a) Aligning the upper waveguides



(b) Aligning the lower waveguides



(c) Interior waveguides aligned with target devices

Figure 5.1: Three-step process for using two single-point couplings to achieve coupling along an arbitrarily large linear array

waveguides, the rotation of the fiber array can be corrected to align the interior fibers to their corresponding waveguides.

Budget

BOM (Bill of Materials)	Unit Cost \$	Unit	# of Units	Total \$	Exact or estimated?
LioniX Interposer	\$ 600.00	1	1	\$ 600.00	Estimated
Thorlabs polarization-maintaining optical circulator	\$ 800.00	1	1	\$ 800.00	Estimated
Various optical fibers	\$ 300.00	1	1	\$ 300.00	Estimated

	Total \$	Exact or estimated?
Total development cost:	\$ 1,700.00	Estimated
What is the minimum cost to make one prototype of your project?	\$ 1,700.00	Estimated
Total cost of items purchased through the Active Learning	\$ -	Exact
Total cost covered by the Laboratory for Nanoscale Optics	\$ 1,700.00	Estimated

Please list below all material used in ALL that were not accounted for in your budget / made available to you at no
Assorted fastener hardware
Small 3D printed parts
Scrap acrylic

Bibliography

- [1] C. C. Davis and T. E. Murphy, "Fiber-optic communications," *IEEE Signal Processing Magazine*, vol. 28, no. 4, pp. 147–150, Jul. 2011. [Online]. Available: <https://ieeexplore-ieee-org.ezp-prod1.hul.harvard.edu/stamp/stamp.jsp?tp=&arnumber=5888645&tag=1> (visited on 09/22/2019).
- [2] X. Chen, M. M. Milosevic, S. Stankovic, S. Reynolds, T. Dominguez Bucio, K. Li, D. J. Thomson, F. Gardes, and G. T. Reed, "The emergence of silicon photonics as a flexible technology platform," *Proceedings of the IEEE*, vol. 106, no. 12, pp. 2101–2116, 2018, ISSN: 0018-9219.
- [3] M. Zhao, W. Kusolthossakul, and K. Fang, *High-efficiency fiber-to-chip interface for aluminum nitride quantum photonics*. 2019, eprint: 1910.13834.
- [4] R. Marchetti, C. Lacava, L. Carroll, K. Gradkowski, and P. Minzioni, "Coupling strategies for silicon photonics integrated chips," *Photon. Res.*, vol. 7, no. 2, pp. 201–239, Feb. 2019. DOI: 10.1364/PRJ.7.000201. [Online]. Available: <http://www.osapublishing.org/prj/abstract.cfm?URI=prj-7-2-201>.
- [5] L. Carroll, J.-S. Lee, C. Scarella, K. Gradkowski, M. Duperron, H. Lu, Y. Zhao, C. Eason, P. Morrissey, M. Rensing, S. Collins, H. Hwang, and P. O'Brien, "Photonic packaging: Transforming silicon photonic integrated circuits into photonic devices," *Applied Sciences*, vol. 6, no. 12, p. 426, 2016, ISSN: 20763417. [Online]. Available: <http://search.proquest.com/docview/1858322667/>.
- [6] L. He, M. Zhang, A. Shams-Ansari, R. Zhu, C. Wang, and L. Marko, "Low-loss fiber-to-chip interface for lithium niobate photonic integrated circuits," *Opt. Lett.*, vol. 44, no. 9, pp. 2314–2317, May 2019, Publisher: OSA. DOI: 10.1364/OL.44.002314. [Online]. Available: <http://ol.osa.org/abstract.cfm?URI=ol-44-9-2314>.
- [7] T. Barwicz, T. W. Lichoulas, Y. Taira, Y. Martin, S. Takenobu, A. Janta-Polczynski, H. Numata, E. L. Kimbrell, J.-W. Nah, B. Peng, D. Childers, R. Leidy, M. Khater, S. Kamlapurkar, E. Cyr, S. Engelmann, P. Fortier, and N. Boyer, "Automated, high-throughput photonic packaging," *Optical Fiber Technology*, vol. 44, pp. 24–35, 2018, ISSN: 1068-5200. DOI: <https://doi.org/10.1016/j.yofte.2018.02.019>. [Online]. Available: <http://www.sciencedirect.com/science/article/pii/S1068520017302225>.

- [8] J. H. Song, P. O'Brien, and F. H. Peters, "Optimal laser welding assembly sequences for butterfly laser module packages," *Opt. Express*, vol. 17, no. 19, pp. 16 406–16 414, Sep. 2009, Publisher: OSA. doi: 10.1364/OE.17.016406. [Online]. Available: <http://www.opticsexpress.org/abstract.cfm?URI=oe-17-19-16406>.
- [9] S. Aghaeimeibodi, B. Desiatov, J.-H. Kim, C.-M. Lee, M. A. Buyukkaya, A. Karasahin, C. J. K. Richardson, R. P. Leavitt, M. Lončar, and E. Waks, "Integration of quantum dots with lithium niobate photonics," *Applied Physics Letters*, vol. 113, no. 22, p. 221102, Nov. 26, 2018, Publisher: American Institute of Physics, ISSN: 0003-6951. doi: 10.1063/1.5054865. [Online]. Available: <https://doi.org/10.1063/1.5054865> (visited on 03/01/2020).
- [10] Thorlabs, *PT3 - 1" XYZ translation stage with standard micrometers, 1/4"-20 taps*, Oct. 17, 2000. [Online]. Available: <https://www.thorlabs.com/thorproduct.cfm?partnumber=PT3#ad-image-2>.
- [11] (). MODE - finite difference eigenmode (FDE) solver introduction, Lumerical Support, [Online]. Available: <https://support.lumerical.com/hc/en-us/articles/360034917233-MODE-Finite-Difference-Eigenmode-FDE-solver-introduction>.
- [12] Z. Zhu and T. G. Brown, "Full-vectorial finite-difference analysis of microstructured optical fibers," *Opt. Express*, vol. 10, no. 17, pp. 853–864, Aug. 2002, Publisher: OSA. doi: 10.1364/OE.10.000853. [Online]. Available: <http://www.opticsexpress.org/abstract.cfm?URI=oe-10-17-853>.
- [13] (). MODE - 2.5d varFDTD solver introduction, Lumerical Support, [Online]. Available: <https://support.lumerical.com/hc/en-us/articles/360034917213-MODE-2-5D-varFDTD-solver-introduction->.
- [14] *Manuals/binary protocol manual*, in *Zaber Wiki*. [Online]. Available: https://www.zaber.com/w/Manuals/Binary_Protocol_Manual.
- [15] P. Clade. (Jul. 28, 2017). ThorlabsPM100 1.1.2, PyPi, [Online]. Available: <https://pypi.org/project/ThorlabsPM100/1.1.2/>.

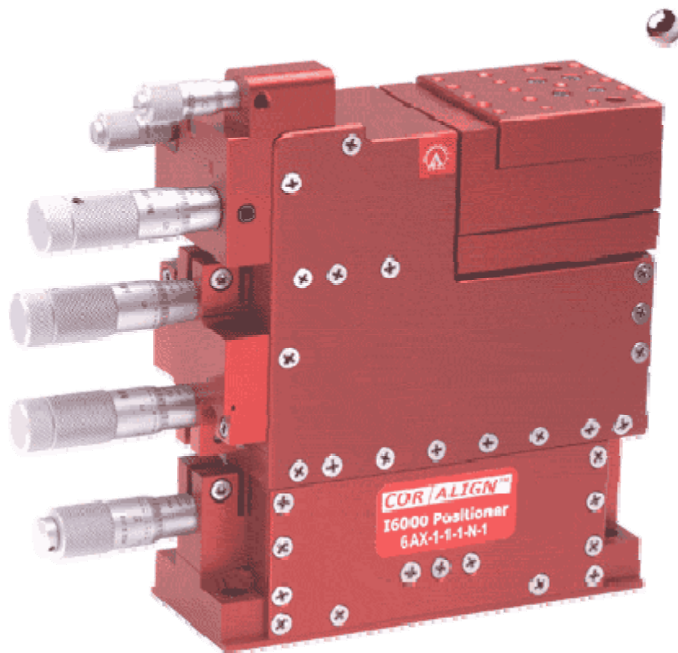
Appendix A

Technical specifications of nanopositioning stage



LUMINOS
INDUSTRIES LTD.

I6000/I6005 6-Axis Positioner User Manual



Revision 7, October 9, 2008
Copyright © Luminos Industries Ltd.

I6000/I6005 6-Axis Positioner User Manual
Getting Started

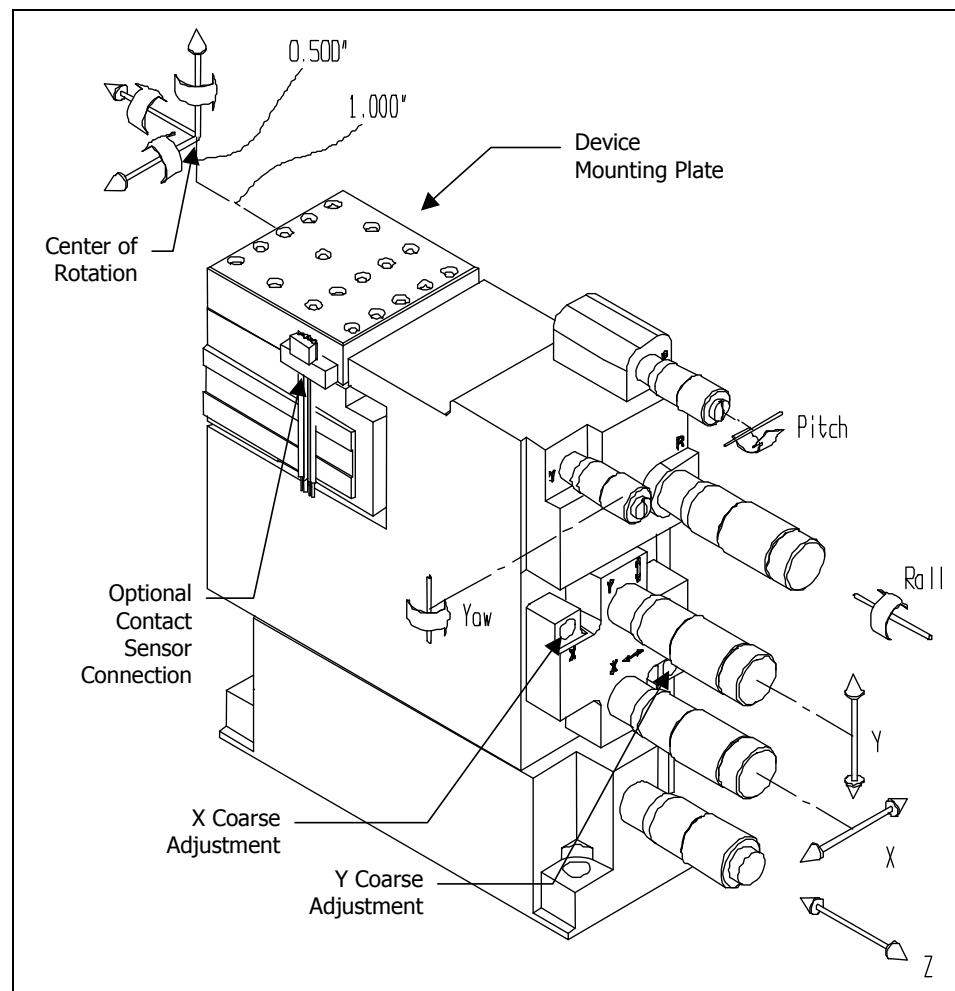


Figure 2 - I6000/I6005 6-Axis Positioner

I6000/I6005 Specifications

Travel			
Axis	Actuator ¹	Coarse	Total
Z – focus	12.7mm (0.5")	N/A	12.7mm (0.500")
I6000	Y – vertical	0.5mm (0.02")	2mm (0.080")
	X – lateral	0.5mm (0.02")	2mm (0.080")
I6005	Y – vertical	2.5mm (0.1")	N/A
	X – lateral	2.5mm (0.1")	N/A
Roll	3 degrees	N/A	3 degrees
Yaw	3 degrees	N/A	3 degrees
Pitch	3 degrees	N/A	3 degrees
Setability ² (Micrometer)			
Axis	Resolution	Movement /Division	
Z	0.25 micron (10μ-inch)	0.001"	
I6000	Y	10nm (0.4μ-inch)	1μm - 25x Ratio Drive™
	X	10nm (0.4μ-inch)	1μm - 25x Ratio Drive™
I6005	Y	50nm (2μ-inch)	5μm - 5x Ratio Drive™
	X	50nm (2μ-inch)	5μm - 5x Ratio Drive™
Roll	0.1 arc sec	10 arc sec	
Yaw	0.2 arc sec	30 arc sec	
Pitch	0.2 arc sec	30 arc sec	
Resolution (Stepper Motor – Type A)			
Axis	Resolution	Total Steps	
Z	100nm (4μ-inch)	128 000	
I6000	Y	4nm (0.16μ-inch)	128 000 - 25x Ratio Drive™
	X	4nm (0.16μ-inch)	128 000 - 25x Ratio Drive™
I6005	Y	20nm (0.8μ-inch)	128 000 - 5x Ratio Drive™
	X	20nm (0.8μ-inch)	128 000 - 5x Ratio Drive™
Roll	0.1 arc sec	101 206	
Yaw	0.2 arc sec	60 416	
Pitch	0.2 arc sec	60 416	
Stage Configuration & Arc Error Motion			
Axis	Flexure Type	Arc Error	
Z	Dual	None - True Linear Motion	
Y	Single	Max 30μm - Arc Error in Z only	
X	Single	Max 30μm - Arc Error in Z only	
Roll	Single	Max 35μm	
Yaw	Dual	None	
Pitch	Dual	None	
Linear Stiffness			
Along Axis	Stiffness	Comments	
Z	130 kN/m	measured at the rotation center	
Y	95 kN/m	measured at the rotation center	
X	40 kN/m	measured at the rotation center	

I6000/I6005 6-Axis Positioner User Manual
What is Ratio Drive™?

Torsional Stiffness		
About Axis	Stiffness	Comments
Z - roll	75Nm/rad	measured at the rotation center
Y - yaw	100Nm/rad	measured at the rotation center
X - pitch	130Nm/rad	measured at the rotation center
Maximum Load		
Static Load	Transient Load	Comments
2.2 lbs (1kg)	10 lbs (4.5kg)	stage must be protected from shock loading during transport and usage
Physical Properties		
Characteristic	Specifications	Comments
Construction	Aluminum	6061 & 7075 - T6 anodized
Weight	1.5kg	Approximate
Body Dimensions	5.79" x 1.75" x 5.19"	LxWxH excluding micrometers
Mounting Height	5.19"	Base to top of mounting plate
Mounting Config. Imperial	0.26" dia. holes	1.00" x 4.00" ³ centers
Mounting Config. Metric	6.6mm dia. holes	25mm x 100mm centers
Concurrent Rotation Center	1/2"	Above top of mounting plate
	1"	Out from end of mounting plate

¹ 'Actuator' refers to a micrometer or stepper motor.

² Operator dependent

³ Compatible with 1.00" grid optical tables, units mount on 2" intervals with 0.25" allowance for routing of cables etc.

What is Ratio Drive™?

Ratio Drive™ is a means of "dividing down" the motion of the actuator to give higher resolution at the output of a positioner stage. This causes the output of the positioner stage to be only a fraction of the movement of the actuator - increasing resolution and decreasing backlash (since no gears are used in the Ratio Drive™). This technique allows the use of a standard micrometer or inexpensive stepper motor for enhanced, high precision alignment. Note: Ratio Drives™ are only on the X and Y axes.

25x Ratio Drive™

With the 25x Ratio Drive™, 12.7mm of micrometer travel is divided down 25.4 times to give 0.5mm of travel at the output plate. Coarse adjustments using an Allen key add an additional 2mm for a total of 2.5mm of travel. With the stepper motor actuator, the X & Y stages achieve a resolution of 4 nanometers on X and Y axes.

Products that incorporate the 25x Ratio Drive™ include the I3000, I5000 and I6000.

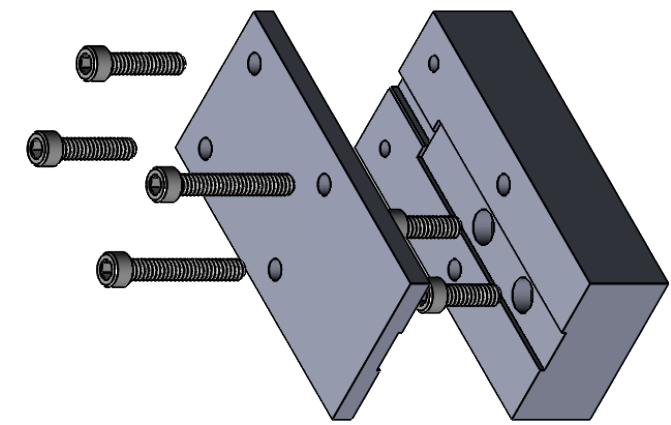
5x Ratio Drive™

A 5x Ratio Drive™ divides the motion down by 5 times so that one 12.7mm of actuator travel becomes 2.5mm at the output. With this option, there are no coarse adjustments

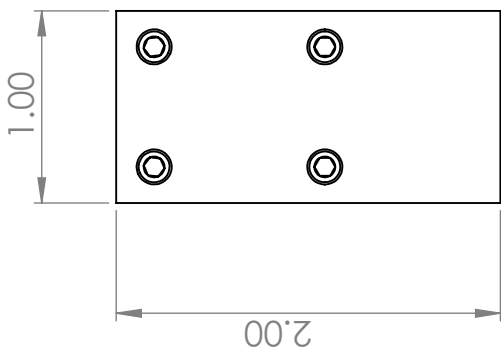
Appendix B

Drawings of interposer clamp

B

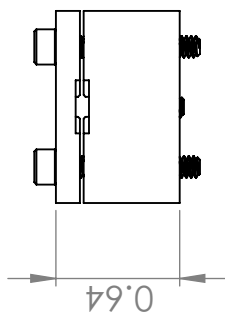


1



B

4-40 Socket Head Cap Screws



53

A

INTERPOSER CLAMP

TITLE:

Q.A.

COMMENTS:

DRAWN

CHECKED

ENG APPR.

MFG APPR.

INTERPRET GEOMETRIC

TOLERANCING PER:

MATERIAL

FINISH

USED ON

APPLICATION

DO NOT SCALE DRAWING

PROPRIETARY AND CONFIDENTIAL
THE INFORMATION CONTAINED IN THIS
DRAWING IS THE SOLE PROPERTY OF
<INSERT COMPANY NAME HERE>. ANY
REPRODUCTION IN PART OR AS A WHOLE
WITHOUT THE WRITTEN PERMISSION OF
<INSERT COMPANY NAME HERE> IS
PROHIBITED.

REV

SIZE

DWG. NO.

A

SCALE: 1:1

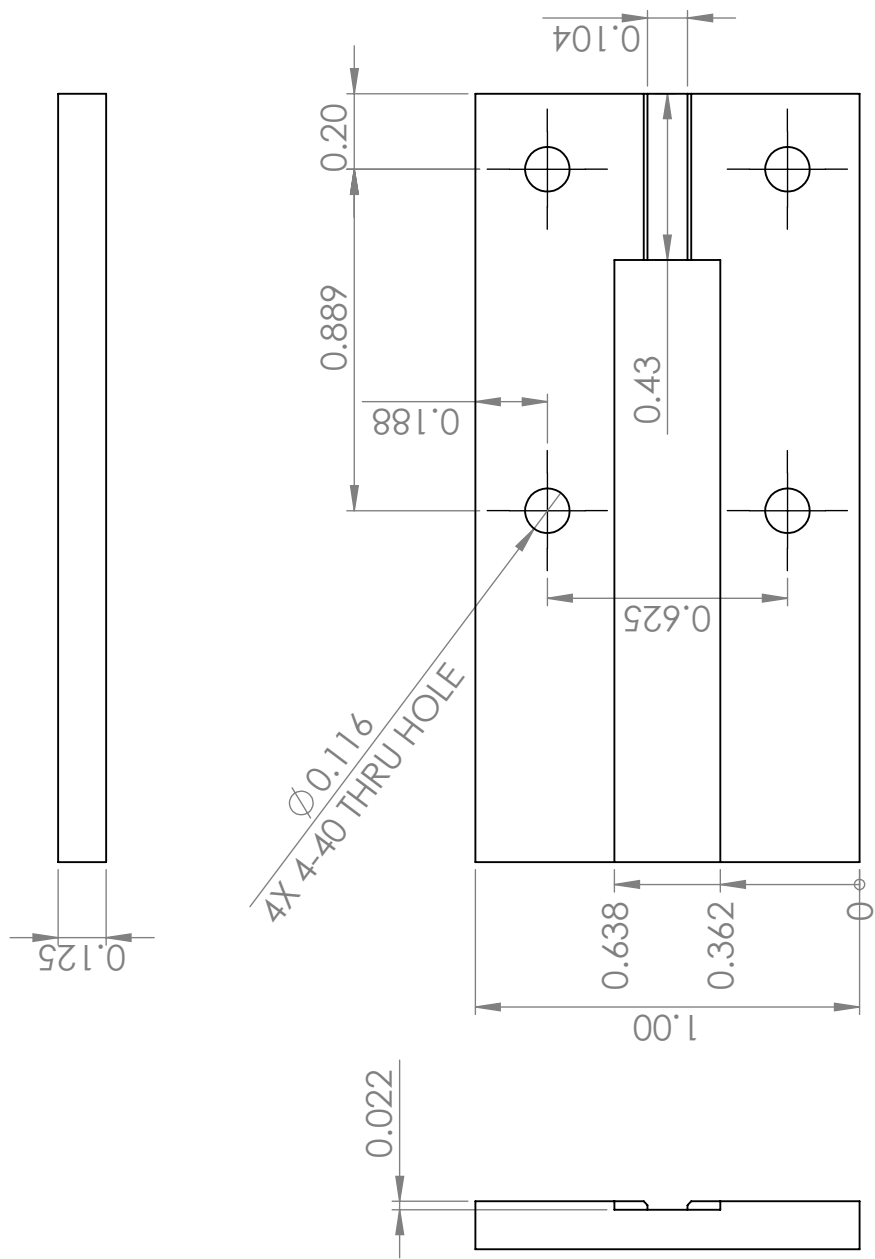
SHEET 1 OF 1

A

A

B

B



UNLESS OTHERWISE SPECIFIED:		<COMPANY NAME>	
DRAWN	NAME	DATE	
CHECKED			TITLE:
ANGULAR: MACH ⁺	BEND [±]		INTERPOSER CLAMP TOP
TWO PLACE DECIMAL [±]	THREE PLACE DECIMAL [±]		
MFG APPR.			
Q.A.			
COMMENTS:			
INTERPRET GEOMETRIC TOLERANCING PER: MATERIAL			
NEXT ASSY	USED ON	FINISH	
APPLICATION		DO NOT SCALE DRAWING	
SIZE	DWG. NO.	REV	
A			
SCALE: 2:1		SHEET 1 OF 1	

PROPRIETARY AND CONFIDENTIAL
THE INFORMATION CONTAINED IN THIS
DRAWING IS THE SOLE PROPERTY OF
<INSERT COMPANY NAME HERE>. ANY
REPRODUCTION IN PART OR AS A WHOLE
WITHOUT THE WRITTEN PERMISSION OF
<INSERT COMPANY NAME HERE> IS
PROHIBITED.

A

INTERPOSER CLAMP BOTTOM

REV

A

SHEET 1 OF 1
SCALE: 3:2

1

<COMPANY NAME>

TITLE:

DRAWN
CHECKED
ENG APPR.
MFG APPR.

Q.A.
COMMENTS:

SIZE DWG. NO. A

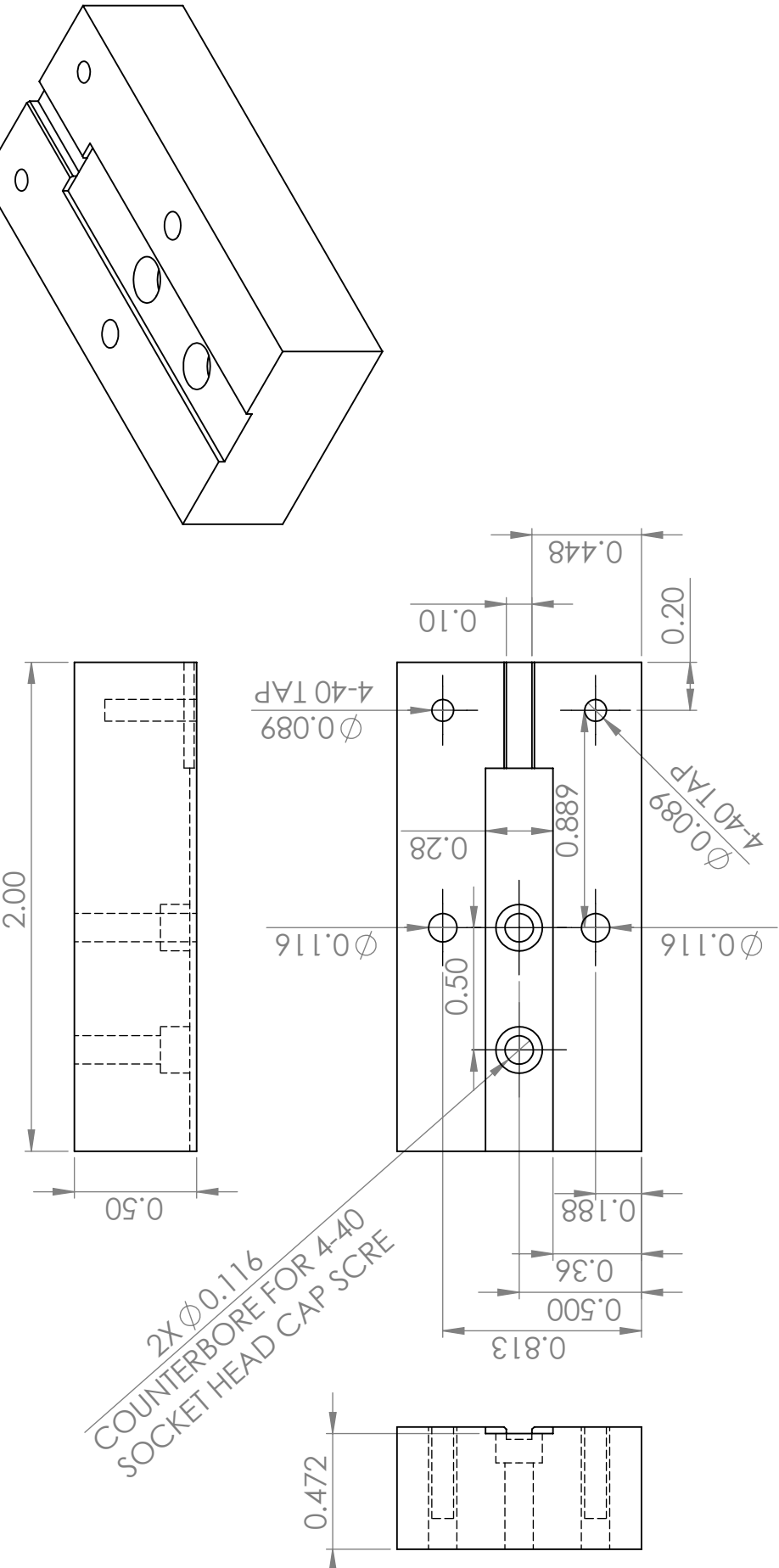
SCALE: 3:2 SHEET 1 OF 1

UNLESS OTHERWISE SPECIFIED: DIMENSIONS ARE IN INCHES TOLERANCES: FRACTIONAL \pm ANGULAR MACH \pm BEND \pm TWO PLACE DECIMAL \pm THREE PLACE DECIMAL \pm	
INTERPRET GEOMETRIC TOLERANCING PER: MATERIAL	
NEXT ASSY	USED ON
APPLICATION	DO NOT SCALE DRAWING
PROPRIETARY AND CONFIDENTIAL THE INFORMATION CONTAINED IN THIS DRAWING IS THE SOLE PROPERTY OF <INSERT COMPANY NAME HERE>. ANY REPRODUCTION IN PART OR AS A WHOLE WITHOUT THE WRITTEN PERMISSION OF <INSERT COMPANY NAME HERE> IS PROHIBITED.	2

A

B

B



Appendix C

Technical specifications of photodiode and power meter

Compact USB Power Meter with Germanium Photodiode Detector

**PM16-122**

Description

The PM16 remotely controlled power meters have USB interfaces and are offered with a selection of photodiode and thermal power sensors. Other sensors are available upon request; please contact Tech Support with inquiries. Each sensor is connected to the USB interface by a standard 1.5 m connection cable and can be operated using any of the software and driver packages that are compatible with Thorlabs' other power meters. The PM16-122 power sensor head is designed for general purpose optical power measurements. The head is optimized for small thickness to fit in tight spaces. The high sensitivity photodiode with large active area in combination with a reflective, diffused ND filter enables power measurements up to 40 mW in free-space and fiber-based applications. A removable annular VIS/IR viewing target serves as an aid for centering a beam on the active area of the photodiode. The target absorbs light from 400 to 640 nm and 800 to 1700 nm.

The front face of the PM16-122 housing is SM1 (1.035"-40) threaded for compatibility with Thorlabs' Ø1" lens tubes and other accessories, providing a convenient way to mount external optics, fiber adapters, light filters, and apertures. A combined 8-32- and M4-threaded mounting hole on the side of the housing accepts both metric and imperial posts.

The meter holds the sensor's individual NIST- and PTB- traceable spectral calibration data in a non-volatile memory.

Software Installation

System Requirements: Windows XP and Later

The PM16 requires a National Instruments VISA installation, that can be downloaded from the National Instruments website (<https://www.ni.com/visa/>), to allow the correct USB installation as an "Test and Measurement Device (IVI)". Please install NI VISA first and then plug the PM16 into a free USB port. Wait until USB installation has finished, after which the device is ready to operate.

Software, drivers, command reference and examples can be downloaded from www.thorlabs.com

Cleaning and Maintenance

There are no serviceable parts in the PM16-122 head. The housing may be cleaned by wiping with a soft damp cloth. When cleaning the aperture filter, treat it as any other fine optic. Gently blow off any debris using compressed air and wipe gently with an optic tissue wetted with propanol. If you suspect a problem with your PM16-122 please call Thorlabs and an engineer will be happy to assist you.

As long as the sensor has not been exposed to excessive optical power (please pay attention to the maximum ratings in the technical specifications), the calibration should be very stable over long

periods of time (well over a year). To keep the accuracy and performance of the PM16-122, Thorlabs recommends a yearly recalibration, starting one year after purchase.

Specifications

PM16-122 Specifications	
Sensor Properties	
Detector Type	Germanium Photodiode
Wavelength Range	700 - 1800 nm
Optical Power Working Range	50 nW - 40 mW
Max Average Power Density	10 W/cm ²
Linearity	± 0.5%
Active Area Uniformity ^a	± 1%
Resolution	<2 nW
Calibration Uncertainty ^a	±5%
Typical Application	
Laser Types	Diode, Diode Arrays, He-Ne, Dye, Ion Lasers (Ar+, Kr+)
Filter / Diffuser	Absorptive ND (Schott NG9)
Response Time	<1 µs
Sensor Head Dimensions	Ø30.5 mm x 12.7 mm
Active Detector Area	9.7 mm x 9.7 mm
Input Aperture	Ø9.5 mm
Post	8-32 & M4 Combined Thread
Aperture Thread	External SM1 (1.035"-40)
Fiber Adapters (Optional)	FC, SC, LC, SMA, ST (Not Included)
Cable Length	1.5 m
Electronics Properties	
Analog Measurement Ranges ^b	500 nA, 50 µA, 5 mA
Measurement Units	W, dBm, A
AD Converter	24 Bit
Analog Amplifier Bandwidth	10 Hz
Update Rate	10/s
Remote Interface	USB 2.0
Power Supply	External: 5 V DC via USB
Connector	USB
Electronics Dimensions	65 mm x 20 mm x 10 mm
Total Weight	0.07 kg

a. Beam diameter > 1 mm

b. The appropriate range is chosen internally by the power meter to achieve the best accuracy; the auto-ranging function can be deactivated.



Appendix D

Lumerical Scripts

D.1 Geometry generation

```
# Create new project
newproject; redrawoff;
clear;

## Chip waveguide
# Container group
addstructuregroup;
set("name", "chip_waveguide");
set("x", 0);
set("y", 0);
set("z", 0);
wafer_width = 20e-6;
wafer_length = 100e-6;

# Buried oxide layer. Top of BOX is z = 0
addrct; addtogroup("chip_waveguide");
set("name", "BOX");
box_thickness = 2e-6;
set("material", "SiO2\u2225(Glass)\u2225Palik");
set("x\u2225min", 0);
set("x\u2225max", wafer_length);
set("y\u2225min", -wafer_width/2);
set("y\u2225max", wafer_width/2);
set("z\u2225min", -box_thickness);
set("z\u2225max", 0);

# Handle wafer
addrct; addtogroup("chip_waveguide");
wafer_thickness = 20e-6;
set("name", "handle_wafer");
set("material", "Si\u2225(Silicon)\u2225Palik");
set("x\u2225min", 0);
set("x\u2225max", wafer_length);
set("y\u2225min", -wafer_width/2);
set("y\u2225max", wafer_width/2);
set("z\u2225min", getnamed("chip_waveguide::BOX","z\u2225min") - wafer_thickness);
set("z\u2225max", getnamed("chip_waveguide::BOX","z\u2225min"));

# LN waveguide
ln_thickness = 600e-9;
lnwg_height = 350e-9;
lnwg_top_width = 1.2e-6;
lnwg_sidewall_angle = pi*70/180;
ln_bottom_width = lnwg_top_width + 2*ln_thickness/tan(lnwg_sidewall_angle);
vtx = [0,0];
```

```

        wafer_width, 0;
        wafer_width, ln_thickness - lnwg_height;
        wafer_width/2 + ln_bottom_width/2, ln_thickness - lnwg_height;
        wafer_width/2 + lnwg_top_width/2, ln_thickness;
        wafer_width/2 - lnwg_top_width/2, ln_thickness;
        wafer_width/2 - ln_bottom_width/2, ln_thickness - lnwg_height;
        0, ln_thickness - lnwg_height];
addpoly; addtogroup("chip_waveguide");
set("name", "LN_waveguide");
set("index", "2.21");
set("x", wafer_length/2);
set("y", -wafer_width/2);
set("z", 0);
set("z_span", wafer_length);
set("vertices", vtx);
set("first_axis", "x");
set("rotation_1", 90);
set("second_axis", "z");
set("rotation_2", 90);

# Cladding
addrct; addtogroup("chip_waveguide");
cladding_thickness = 2e-6;
set("name", 'cladding');
set("material", "SiO2(Glass)-Palik");
set("x_min", 0);
set("x_max", wafer_length);
set("y_min", -wafer_width/2);
set("y_max", wafer_width/2);
set("z_min", 0);
set("z_max", ln_thickness + cladding_thickness);
set("override_mesh_order_from_material_database", true);
set("mesh_order", 3);

## Interposer waveguide
# Container group
addstructuregroup;
set("name", "interposer_waveguide");
set("x", 0);
set("y", 0);
set("z", 0);
ip_len = 10e-6;
ip_width = 10e-6;
ip_box_thickness = 8e-6;
ip_cladding_thickness = 15e-6;

# Substrate
addrct; addtogroup("interposer_waveguide");
set("name", "substrate");
# set("material", "SiO2 (Glass) - Palik");
set("index", 1.44);
set("x_min", -ip_len);
set("x_max", 0);
set("y_min", -ip_width/2);
set("y_max", ip_width/2);
set("z_min", -ip_box_thickness);
set("z_max", ip_cladding_thickness);
set("override_mesh_order_from_material_database", true);
set("mesh_order", 3);

# Trapezoidal waveguides
ipwg_top_wid = 1.2e-6;
ipwg_sidewall_angle = pi*82/180;
ipwg_thickness = 170e-9;
ipwg_bot_wid = ipwg_top_wid + 2*ipwg_thickness/tan(ipwg_sidewall_angle);
ipwg_spacing = 500e-9;
addobject("isos_trpzd_extpoly");
set("name", "bottom_wg");

```

```
set("index", 1.9963);
set("x", -ip_len/2);
set("y", 0);
set("z", ipwg_thickness/2);
set("lx_top", ipwg_top_wid);
set("lx_base", ipwg_bot_wid);
set("y_span", ipwg_thickness);
set("z_span", ip_len);
set("first_axis", "x");
set("rotation_1", 90);
set("second_axis", "z");
set("rotation_2", 90);
copy(0,0,ipwg_spacing + ipwg_thickness/2);
set("name", "top_wg");
```

D.2 FDE scripting

```
# Clear everything
cleardcard;
clear;
# Create structures and establish geometry
geometry;

# Create FDE solver
addfde;
set("solver_type", "2D_X_normal");
set("x", 0);
set("y", 0);
set("z", 0);
set("y_span", 8e-6);
set("z_span", 8e-6);
set("define_y_mesh_by", "maximum_mesh_step");
set("define_z_mesh_by", "maximum_mesh_step");
set("dy", 50e-9);
set("dz", 50e-9);
set("y_max_bc", "PML");
set("y_min_bc", "PML");
set("z_max_bc", "PML");
set("z_min_bc", "PML");
set("search", "near");
set("use_max_index", false);
set("n", 2.21);
setanalysis("wavelength", 1550e-9);

# Disable interposer
select("interposer_waveguide");
set("enabled", false);

# Find fundamental mode of chip waveguide
findmodes;
copydcard("mode1", "chip_wg_mode");
switchtolayout;

# Disable chip and enable interposer
select("interposer_waveguide");
set("enabled", true);
select("chip_waveguide");
set("enabled", false);

# Find fundamental mode of interposer waveguide
select("FDE");
set("n", 1.53);
findmodes;
copydcard("mode1", "interposer_wg_mode");

# Calculate overlap as a function of shift
zshift = -2e-6:5e-8:2e-6;
yshift = -2e-6:5e-8:2e-6;
power_coupling = zeros(length(zshift), length(yshift));
for (ii = 1:length(zshift)) {
    for (jj = 1:length(yshift)) {
        out = overlap("interposer_wg_mode", "chip_wg_mode", 0, yshift(jj), zshift(ii));
        power_coupling(ii,jj) = out(2);
    }
}
matlabsave("FDEresults01", yshift, zshift, power_coupling);
```

D.3 varFDTD scripting

```

# Clear everything
cleardcard;
clear;
# Create structures and establish geometry
geometry;

# Shift interposer down a little to optimize coupling
select("interposer_waveguide");
set("z", -0.1e-6);

# Create varFDTD solver
addvarfdtd;
set("x_min", -8e-6);
set("x_max", 96e-6);
set("y_min", -6e-6);
set("y_max", 6e-6);
set("z_min", -6e-6);
set("z_max", 6e-6);
set("x_min_bc", "PML");
set("x_max_bc", "PML");
set("y_min_bc", "PML");
set("y_max_bc", "PML");
set("z_min_bc", "PML");
set("z_max_bc", "PML");
set("x0", -48e-6);
set("y0", 0);

# Add a source
addmodesource;
set("name", "source");
set("x", -5e-6);
set("set_wavelength", true);
set("center_wavelength", 1550e-9);
set("wavelength_span", 30e-9);
set("y", 0);
set("y_span", 5e-6);

# Add monitor
addpower;
set("name", "monitor");
set("monitor_type", "2D_X-normal");
set("x", 50e-6);
set("y", 0);
set("y_span", 4e-6);
set("z", 0);
set("z_span", 4e-6);

# Rotate everything
select("chip_waveguide");
set("first_axis", "x");
set("rotation_1", 90);
select("interposer_waveguide");
set("first_axis", "x");
set("rotation_1", 90);

if false {
##Run with simulation with the chip at different positions
# relative to the interposer
N = 32; # Number of x (axial) positions
M = 13; # Number of y (transverse) positions
xmax = 5e-6;
ymax = 2e-6;
dx = linspace(0, xmax, N);
}

```

```

dy = linspace(ymax,-ymax,M);
Ts = zeros(N,M);
for (ii = 1:N) {
    for (jj = 1:M) {
        # Run simulation and store results in Ts
        run;
        R = getresult("monitor","T");
        Ts(ii,jj) = R.T(3);

        switchtolayout;
        # Move chip waveguide and monitor
        select("chip_waveguide");
        set("x", dx(ii));
        set("y", dy(jj));
        select("monitor");
        set("x", 50e-6 + dx(ii));
        set("y", dy(jj));
    }
}

image(dx,dy,10*log10(Ts));
matlabsave("varFDTDresults_04",dx,dy,Ts);
}

```

Appendix E

Python module for interfacing with the nanopositioning stage

```
#####
# Class for controlling a Luminos I6000 or I6005 stage via serial
#
# By Alexander Giglio for the Loncar Lab
# agiglio@college.harvard.edu
# Created on 2019-10-30
#
#####
import zaber.serial as zs
import numpy as np

class I600X:
    # Actuator name to Zaber device number mappings
    a2n = {'X': 2, 'Y': 3, 'Z': 1, 'ROLL': 4, 'PITCH': 6, 'YAW': 5}
    # List to hold maximum range of actuators in microsteps
    maxRangeSteps = {'X': 128000, 'Y': 128000, 'Z': 128000,
                      'ROLL': 101206, 'PITCH': 60416, 'YAW': 60416}
    # List to hold maximum ranges of actuators in physical units.
    # Linear distances given in microns, angles given in degrees
    maxRangeReal = {'X': 500, 'Y': 500, 'Z': 12700,
                     'ROLL': 3, 'PITCH': 3, 'YAW': 3}
    # Dictionary to hold actuators
    actuators = {}
    # Dictionary to hold actuator positions in microsteps
    microsteps = {}
    # Dictionary to hold stage position in microns and degrees
    position = {}

    # Initialize stage at port. Usually COM3
    def __init__(self, port):
        self.port = zs.BinarySerial(port)
        # Fill actuator dictionary
        for axis in self.a2n.keys():
            self.actuators[axis] = zs.BinaryDevice(self.port, self.a2n[axis])

    # Home stage. This sets all actuators to microstep coordinate 0
    def home_stage(self):
        print("Homing stage...")
        command = zs.BinaryCommand(0, 1)      # Command to home all devices
        self.port.write(command)              # Send command to device

        # Keep reading until all devices have replied that they are home
        homing_status = np.array([0, 0, 0, 0, 0, 0])
        while True:
```

```

        reply = self.port.read()
        dn = reply.device_number
        cn = reply.command_number
        if cn == 1:
            homing_status[dn-1] = 1
        else:
            Exception('Stage was unable to go home.')
            return -1
    if homing_status.sum() == 6:
        for axis in self.a2n.keys():
            self.microsteps[axis] = 0
            self.position[axis] = self.steps2real(axis, 0)
        print('Stage at home')
        return 0

# Sets all actuators to half their maximum microstep position
# Returns 0 when stage is centered
def center_stage(self):
    print('Centering stage...')
    # Set all actuators to their center positions
    for axis in self.a2n.keys():
        # UnexpectedReply errors will shut this down for some reason
        try:
            # Move actuator halfway to its max position
            reply = self.actuators[axis]\.
                move_abs(self.maxRangeSteps[axis] // 2)
            # Keep reading from serial until the actuator is done
            while reply.command_number != 20:
                reply = self.port.read()
            # Store position of actuators in dictionary
            self.microsteps[axis] = reply.data
            self.position[axis] = self.steps2real(axis, reply.data)
        except zs.UnexpectedReplyError:
            pass
    print('Stage centered')
    return 0

# Returns 0 upon stopping all actuators from moving. Has the benefit of
# reading all replies in device buffer.
def stop_all(self):
    for axis in self.a2n.keys():
        try:
            reply = self.actuators[axis].stop()
            while reply.device_number != self.a2n[axis] or\
                reply.command_number != 23:
                reply = self.port.read()
            self.microsteps[axis] = reply.data
        except zs.UnexpectedReplyError:
            pass
    return 0

# Move actuator to desired position in microsteps and stops all actuators.
# Returns 0 upon success.
def actuate(self, axis, steps):
    if axis not in self.a2n.keys():
        raise Exception('Invalid actuator')
    try:
        reply = self.actuators[axis].move_abs(steps)
        while reply.device_number != self.a2n[axis] or\
            reply.command_number != 20:
            reply = self.port.read()
        self.microsteps[axis] = reply.data
        self.stop_all()
    except zs.UnexpectedReplyError:
        pass
    return 0

# Move stage to desired position and orientation in space

```

```

# Real distances given in microns, real angles given in degrees
# Takes as an argument a dictionary with keys corresponding to axes and
# values corresponding to desired position
def orient(self, orientation):
    for axis in orientation.keys():
        if axis in self.actuators.keys():
            self.actuate(axis, self.real2steps(axis, orientation[axis]))
            self.position[axis] = self.steps2real(axis, self.microsteps[axis])

# Convert from actuator microsteps to real position/orientation units
def steps2real(self, axis, steps):
    return steps*self.maxRangeReal[axis]/self.maxRangeSteps[axis]\
           - self.maxRangeReal[axis]/2

# Convert from real position/orientation units to actuator microsteps
def real2steps(self, axis, d):
    return int((d + self.maxRangeReal[axis]/2)*self.maxRangeSteps[axis]\
               / self.maxRangeReal[axis])

# Close serial connection
def close(self):
    self.port.close()

# Close serial connection to stage upon deletion
def __del__(self):
    self.port.close()

```